1290

UNIVERSIDADE Đ
COIMBRA

Bárbara de Matos

INVESTIGATION OF INORGANIC SCINTILLATOR DETECTORS WITH PHOTODIODE READOUT

VOLUME 1

Dissertação no âmbito do Mestrado em Engenharia Física orientada pelo Professor Doutor Rui Miguel Curado da Silva, pelo Professor Doutor Rami Vainio e pelo Doutor Philipp Oleynik e apresentada ao Departamento de Física da Faculdade de Ciências e Tecnologia.

Julho de 2022

It's a magical world, Hobbes, ol' buddy… Let's go exploring!

Bill Watterson, *It's a Magical World: A Calvin and Hobbes Collection*

Acknowledgments

Firstly, I wish to express my most sincere appreciation towards my supervisors. To Professor Rui Curado Silva for the guidance on thesis writing. To Professor Rami Vainio for all the orientation during my stay at University of Turku and help in thesis writing. Finally, to Postdoctoral Researcher Philipp Oleynik for the endless patience, positivism and his crucial support since the lab work in University of Turku until all process of thesis writing. I thank him for being such a source of science and motivation.

In addition to my supervisors, I would like to express my sincere appreciation to Risto Punkkinen and Tatu Peltola for all the help in the clean room of ICT, which was indispensable in the completion of this project.

My stay in Turku was an amazing experience in an academic and personal way. I learned a lot of practical techniques related to the development of space radiation scintillators detectors, having always in mind a trade of between efficiency, signal to noise ratio, power consumption, size price and time.

During my stay in Finland, I have met fantastic people. If it's true that we are made by pieces of people we meet in life, I hope I've kept a big brick of Ceci, Lucy, Miguel and Anna in myself. This trip was a lesson about facing fears and it deeply motivated me to get around my fears and start travelling the world. There is always a place for us, everywhere.

Besides that, I wish to express my special gratitude to my parents, whose love and support are the cornerstones for all my achievements. In addition, I thank to my sister, brother and the rest of the family, that always remind me how amazing it is to be back home.

Also, I would like to properly thank Pedro Sousa and Dr. Jerôme Mendes for their help in thesis writing and for all their support and understanding related to this work, during our research projects. Finally, I deeply wish to thank Sofia, Maria, Hugo, Jorge, Cláudia, Catarina, Zé and André for their everyday support and beautiful friendship.

To my grandparents

Abstract

Van Allen radiation belts are located around the Earth and affect operation of spacecrafts and several satellites that have impact on different aspects of our daily lives. These include communication, satellite navigation, remote sensing, etc. Van Allen belts are composed by energetic charged particles whose dynamics are not completely described and understood.

Radiation detectors on board satellites with orbital paths within the Van Allen belts are very important contributors for the description of particles dynamic phenomena within these belts. Detectors based on inorganic scintillator crystals allow for low noise and high efficiency solutions. LYSO:Ce and GAGG:Ce are two new scintillator crystals with high stopping power, light yield and small decay time with huge potential applications in space instrumentation. However, these crystals present high refractive indexes which leads to multiple reflection losses.

This thesis presents a study on inorganic scintillator crystals that will contribute to the development of detector for electrons and protons called Relativistic Electron and Proton Experiment (REPE). The main goal of this work was to select components for an inorganic scintillation radiation detector in order to optimize light collection and energy resolution, reducing light losses. The components to select include the crystal (LYSO:Ce or GAGG:Ce), the wrapping material, the readout system and the optical matching material (between the crystal and readout system).

This was accomplished by mounting seven detectors in different combinations of components, followed by comparison of their performance in gamma-ray energy detection from a ^{137}Cs source. In this case the performance parameters were obtained through spectroscopy. These are photopeak position and photopeak FWHM, reflecting light collection and energy resolution, respectively.

The inorganic scintillator detector that presented the best performance was composed by GAGG:Ce crystal, unsealed photodiode (S3590-09 series by Hamamatsu), NOA 169 glue (by Norland Products) and teflon wrapping. This combination presented 82.8 % better light collection, and 36.6 % better energy resolution compared to the worst combination evaluated (LYSO:Ce, sealed photodiode - S3590-08 series by Hamamatsu, silicon grease and aluminized kapton wrapping). This work resulted in an inorganic scintillator detector with high light collection, good energy resolution, good sensitivity, small dimensions and low power consumption.

Resumo

As cinturas de radiação de Van Allen estão localizadas em torno da Terra e afetam a operação de aeronaves e de satélites que têm impacto em diversos aspetos da nossa vida quotidiana. Estes incluem comunicação, navegação por satélite, sensores remotos, etc. As cinturas de Van Allen são constituídas por partículas carregadas e aceleradas, cuja dinâmica ainda não está completamente descrita e compreendida.

Os detectores de radiação de satélites em órbita nas cinturas de Van Allen constituem uma importante contribuição para a descrição dos fenómenos dinâmicos das partículas desta cintura. Os detectores baseados em cristais de cintiladores inorgânicos permitem soluções de baixo ruído e elevada eficiência. LYSO:Ce e GAGG:Ce são dois novos cristais cintiladores com elevado poder de paragem, alta eficiência e reduzido tempo de decaimento com enormes potenciais aplicações na instrumentação espacial. Contudo, estes cristais apresentam índices de refracção elevados que conduzem a perdas de luz por reflexões.

Esta tese apresenta um estudo sobre cristais cintiladores inorgânicos que contribuirá para o desenvolvimento de uma experiência chamada Relativistic Electron and Proton Experiment (REPE). O principal objectivo deste trabalho foi selecionar componentes para um detector de radiação de cintilação inorgânica a fim de otimizar a recolha de luz e a resolução de energia, reduzindo as perdas de luz. Os componentes a seleccionar incluem o cristal (LYSO:Ce ou GAGG:Ce), o material de revestimento, o sistema de leitura e o material de transferência ótica (entre o cristal e o sistema de leitura).

Isto foi conseguido através da montagem de 7 detectores constituídos por diferentes combinações de componentes, seguida da comparação do seu desempenho na detecção de energia de raios gama com origem de uma fonte de ^{137}Cs. Neste caso, os parâmetros de desempenho foram obtidos através de espetroscopia. Estes parâmetros são a posição de fotopico e o FWHM de fotopico, refletindo a recolha de luz e a resolução de energia de cada detetor, respetivamente.

O detetor cintilador inorgânico que apresentou o melhor desempenho foi constituído pelo cristal GAGG:Ce, pelo fotodiodo sem janela de resina de silício (série S3590-09 da Hamamatsu), pela cola NOA 169 (da Norland Products) e pelo invólucro de teflon. Esta combinação apresentou 82.8 % melhor recolha de luz, e 36.6 % melhor resolução de energia em comparação com a pior combinação avaliada (LYSO:Ce, fotodíodo com janela -série S3590-08 da Hamamatsu, graxa de silício e revestimento de kapton aluminizado). Este trabalho resultou num detetor cintilador inorgânico com alta recolha de luz, boa resolução de energia, elevada sensibilidade, pequenas dimensões e baixo consumo de energia.

List of Figures

List of Tables

Contents

Chapter 1

Introduction

Motivation and objectives

Since the dawn of humanity, human beings have been trying to understand the phenomena that occur in space. Particularly in recent years, the near-Earth environment has been a special focus of scientists' attention, as it affects technologies that are very present in our daily lives. Satellite navigation, communication, and remote sensing are some examples of these technologies. Our dependence on these systems has immensely grown in the last decades with the rise of the number of satellites operating in the Earth orbit. Therefore, it is crucial to understand the space weather phenomena [28].

During the space era in 1957–1958, a series of space probes discovered that Planet Earth is surrounded by an inner and a outer Van Allen radiation belts. They consist of two trapped particle clouds, whose dynamics depends on solar activity. Van Allen radiation belts include energetic charged particles such as protons and electrons, which can cause satellite malfunctions by altering semiconductor devices and dielectric materials properties or flipping bits in the computer memory. In recent years, with NASA's Van Allen probes, the understanding of the Van Allen belt has been greatly boosted. However, some phenomena that occur in this belt are still posed as mysteries to the scientific community.

Satellites shed light on major advances in space research measurements, including near-Earth environmental research. In particular, there has recently emerged the CubeSat project, which is a new satellite standard that allows these instruments to be small (10 cm x 10 cm x 10 cm) and power-efficient. In this way, CubeSats do not depend on the dimensional characteristics of the launch vehicle, cost less than 1 million, and take less time to develop than conventional satellites. This new form of technology has facilitated and boosted the development of nanosatellites for space research by universities around the world.

University of Turku together with Aalto University, University of Helsinki and Finnish Meteorological Institute, in the frame of the Finnish Center of Excellence in Research of Sustainable Space, proposed a project called FORESAIL, consisting of three CubeSats to be launched into orbit in the Van Allen radiation belts.

The FORESAIL-2 mission is the second CubeSat to be launched within FORESAIL project and will carry the Relativistic Electron and Proton Experiment (REPE). REPE is a radiation detector instrument that has the scientific objective of measuring the energy spectrum of electrons and protons, and monitoring the dynamics of the most intense regions of the Van Allen radiation belts. FORESAIL-2 CubeSat has a planned orbit with a perigee altitude of several hundred kilometers and an apogee altitude of about 36000 km (the geostationary transfer orbit).

REPE instrument consists of a stack of silicon detectors and a scintillator crystal with photodiode readout, in a telescope structure design, with a collimated aperture. The silicon detectors and scintillator detector together, aim to detect electrons in the energy range of 0.3 MeV to 8

MeV and protons up to 70 MeV, by measuring the energy deposited in each detector by the incident particle.

This thesis aims to contribute to REPE development and optimization through the study of inorganic scintillator crystals with photodiode readout. The two main focuses of the present work are the following:

- Study of inorganic scintillators LYSO:Ce and GAGG:Ce for high energy radiation detection
- Select the components for an inorganic scintillation radiation detector, in order to optimize light collection and energy resolution. The components include the crystal, wrapping material, readout system and optical matching material between the crystal and readout system.

As functional requirements, the resultant scintillator detector shall be able to detect incident electrons with energies between 300 keV and 8 MeV, and protons up to 70 MeV, generating current signals proportional to the deposited energy in the crystal. This deposited energy can be from zero until incident energy. This means that the sensitivity of the scintillator detector to the deposited energy in the crystal shall be as low as possible, and lower than 300 keV. In addition, the non-functional requirements for the resultant detector developed in this work are small dimensions (few cm^3), high efficiency, good energy resolution (below 20% $<$ 1 MeV), low noise, low power consumption (hundreds of mW) and low cost scintillator radiation detector.

This study approaches the performance comparison of two new scintillator crystals, LYSO:Ce and GAGG:Ce, addressing different wrapping, two different PIN photodiode models as readout system and different optical media between the crystal and the photodiode. A total of 7 different combinations were evaluated and compared as a function of light collection and energy resolution, in order to choose the best combination.

Main contributions

LYSO:Ce and GAGG:Ce crystals are becoming very attractive scintillators due to their high atomic number and density, ensuring high efficiency, added to other advantages. They have been already implemented in various commercial products of different areas. Although LYSO:Ce and GAGG:Ce have been considered promising scintillators with potential application in future space satellite missions, their application was not widely explored, specially GAGG:Ce [45].

The main practical application of the presented work is its contribution to REPE detector, that aims at a better understanding of Van Allen radiation belt. Although REPE will not use the detector developed in this work directly, because it will add silicon detector layers, it will use the selected best combination of materials for the scintillator part. In addition, it has potential applications in other future CubeSat or nanosats radiation detection space missions. In addition, the present study will also contribute for a performance comparison of LYSO:Ce and GAGG:Ce crystals, as gamma rays and energetic protons and electrons detectors.

Thesis structure

This thesis is divided into seven main chapters. Chapters 1, 2 and 3 consist of an introduction to provide an easier understanding of the rest of the document. Chapter 2 contains the state of the art on Van Allen radiation belt, high energy radiation detectors for space applications, scintillator crystals and readout systems. The third chapter contains important concepts and physic principles which will be useful later on. Chapter 4 presents an analysis of the comparative light collection for several different detector setups, based on theoretical principles.

Thereafter, Chapter 5 describes the experimental and data analysis methods. Chapter 6 shows the experimental results of the relative light collection and energy resolution for the combinations studied in Chapter 4 and compares the results with the expected from the theoretical approach. Possible further improvements are presented in this chapter as well. Chapter 7 has a final conclusion and discusses future perspectives related to this work.

Chapter 2

Main concepts and principles

In order to easily understand the following chapters, a brief approach of important basic concepts and principles will be presented in this section. It begins with an explanation of the main mechanisms of heavy charged particles and gamma-ray interactions with matter, followed by a brief discussion of the scintillation phenomenon. The short description on PIN photodiode operation is given next, as it will be the readout of scintillator crystals. Thereafter, the main scintillator detector general properties are presented, as decay time, detection efficiency, energy resolution, sensitivity and noise and others. Fresnel and Snell equations rule the light interface mechanisms between different surfaces and, as such, will also be quickly approached.

2.1 Interaction of charged heavy particles with matter

Let's consider charged particles heavier than the electron, such as protons, α-particles, ions, pions, muons, etc, passing through matter. The main particle-matter interaction mechanisms are characterized by inelastic collisions between the particle and the atomic electrons of the material, or elastic scattering of the particle from the material nuclei. These reactions occur many times in the particle track inside the matter, and thus, the penetration depth of heavy charged particle inside a crystal is short compared to electrons.

Stopping power

In 1932, Hans Bethe performed quantum mechanic calculations to describe the energy transfer of the relativistic charged particles in an absorbing material, per path length. This quantity is called Linear Energy Transfer ($\frac{-dE}{dx}$), and when presented in terms of energy loss of the charged particle per g cm^{-2} of the medium traversed, it's called Stopping Power (S). The obtained formula for Linear Energy Transfer is [22]:

$$\frac{-dE}{dx} = 2\pi N_a r_e^2 m_e c^2 \rho \frac{Z}{A} \frac{z^2}{\beta^2} \left[\ln\left(\frac{2 m_e \gamma^2 v^2 W_{max}}{I^2}\right) - 2\beta^2 \right] \tag{2.1}$$

where

N_a: Avogadro's number

r_e: classical electron radius

m_e: electron mass

ρ: density of absorbing material

Z: atomic number of absorbing material

A: atomic weight of absorbing material

z: charge of incident particle in units of e

β: v/c of the incident particle

γ: $1/\sqrt{1-\beta^2}$

W_{max}: maximum energy transfer in a single collision

I: mean excitation potential

The energy loss is dependent on charge and the energy of the incident particle, as seen by the dependence on z and β respectively. In a general way, dE/dx is smaller for larger energies. This means more energy per unit length in deposited towards the end of a particle path, rather than at its beginning. In addition, an important consequence of different particles having different stopping power in different materials, is the possibility to distinguish the type of particle by comparing the combination of energy deposited in each material.

The Bethe formula assumes the incident particle has energy high enough so that charge exchange between the particle and the absorber is not important. For smaller energies the positive particle tends to carry electrons, and this reduces its charge effectively, reducing the linear energy loss. The Bethe description's accuracy can be improved by considering corrections which correspond to higher powers of z, instead of z^2. Felix Bloch suggested a correction based on dE/dx proportionality with z^4. In addition, other usual correction consists of taking into account that the atomic electrons of the material are not stationary ("shell correction") [22].

Bethe formula describes well the stopping power, with few percentage error, especially for protons and nuclei up to α-particle with high energy ($\beta \geq 0.1$), that is the case of REPE conditions.

Energy straggling

When a beam of monoenergetic charged particles passes through a certain thickness of absorbing material, a spread in energies always occurs, due to somewhat random variations of the microscopic interactions (see Figure 2.1). This phenomenon is called Energy straggling and depends on whether the particle collides with a nucleus or passes through it without collision. The energy straggling is measured by the width of this energy (E) distribution f(E,X) and varies with the distance (X) along the particle track.

2.2 Interaction of fast electrons with matter

When fast electrons pass through an absorbing material, they lose their energy at a lower rate, compared with heavy charged particles, because electrons mass is much smaller ($\approx$ 2000 times compared to the proton). In addition, they follow a much more tortuous path and reaches a longer distance on average within the crystal, for the same incident energy. An electron generally suffers large deviations in its path because its mass is equal to the mass of the orbital electrons and a large fraction of its energy can be lost in a single interaction. In addition, when electron-nuclear interactions occur, they can provoke an abrupt change the electron direction [17].

Bethe derived an expression similar to Equation 2.1 to describe the specific energy loss due to ionization and excitation (the "collisional losses") for fast electrons:

$$\left(\frac{-dE}{dx}\right)_c = \frac{2\pi e^4 NZ}{m_0 v^2}\left[ln\frac{m_0 v^2 E}{2I^2(1-\beta^2)} - ln2(2\sqrt{1-\beta^2}-1+\beta^2)+(1-\beta^2)+\frac{1}{8}(1-\sqrt{1-\beta^2})^2\right]$$

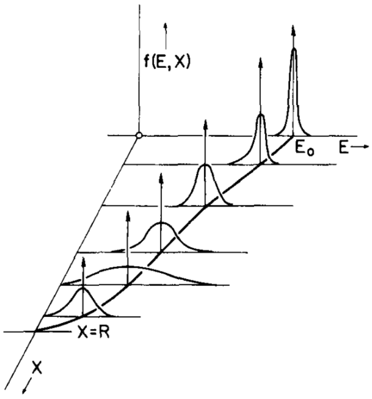

Figure 2.1: General representation of energy straggling of heavy charged particles during their track within matter. E_0 is the initial energy and R is the longest distance the particle reaches. Image from [17].

Furthermore, electrons also differ from heavy charged particles because their energy may be lost by radiative processes and Coulomb interactions. These radiative losses take the form of bremsstrahlung or electromagnetic radiation, which can be emitted from any position along the electron track. The radiative process occurs as a result of electron accelaration when deflected in its interactions with the absorber. The linear specific energy loss through this radiative process was also derived:

$$\left(\frac{-dE}{dx}\right)_r = \frac{NEZ(Z+1)e^4}{137m_0^2c^4}\left(4ln\frac{2E}{m_0c^2} - 4/3\right)$$

The total linear stopping power for electrons is the sum of the collisional and radiative stopping powers (Equation 2.2). Radiative losses are always a small fraction of the energy losses due to ionization and excitation, being only significant for absorbing materials with high atomic number.

$$\frac{dE}{dx} = \left(\frac{dE}{dx}\right)_c + \left(\frac{dE}{dx}\right)_r \tag{2.2}$$

2.3 Interaction of gamma-rays with matter

Gamma-ray and X-ray photons interact with matter through mechanisms that are different from charged particles interaction processes. For photons, interaction probability is lower as they do not suffer Coulomb interactions, reaching longer distances inside the crystal, for the same incident energy. On the other hand, gamma-rays usually lose a large fraction of their energy in one interaction, contrary to charged heavy particles that interact multiple times on their track.

Three main mechanisms rule the interactions of gamma ray photons, with the matter: photoelectric absorption, Compton scattering and pair production. These mechanisms lead to a partial or total transfer of the photon energy to electrons and, for that reason, electrons are in the origin of the main photons detection processes. These phenomena result in the vanishment of the photon or in its scattering through a significant angle. The dominance of one of these mechanism over the other depends on the energy of the gamma ray and on the characteristics of the target material [17].

Photoelectric absorption

In the photoelectric absorption, a photon is absorbed by an atom and it results in the ejection of a photoelectron with an certain energy from one of its bound shells. As a consequence, the photon completely disappears. Photoelectric absorption requires that the incident photon has sufficient energy for the removal of the electron. When the light has enough energy, the photoelectron is ejected with an energy given by:

$$E_e = hv - E_b \tag{2.3}$$

where

E_b: binding energy of the photoelectron in its atom shell

h: Plank's constant

v: frequency of the incident photon

As a consequence of the emission of a photoelectron, an ionized absorber atom with a vacancy is produced. This atom can quickly capture an electron from other shells of the atom or capture a free electron from the medium to fill the vacancy. With this capture, one or more characteristic X-ray photons may be generated.

For gamma rays of relatively low energy ($\leq$ 1 MeV), the photoelectric absorption is the predominant mechanism of interaction with matter. The probability of occurrence of this process also increases for absorber materials of high atomic number Z. An approximated expression for the probability of photoelectric absorption per atom over all ranges of gamma ray energy E_γ and Z is:

$$\tau \approx constant * \frac{Z^n}{E_\gamma} \tag{2.4}$$

being n an exponent that varies between 4 and 5 over the gamma-ray energy region.

Compton scattering

In Compton scattering process, the incoming gamma ray photon is deflected by an electron in the target material. The incident photon is scattered through an angle θ with respect to its original direction, and all angles are possible (from 0 to π). The electron is recoiled by an angle ϕ. The fraction of the incoming photon energy (hv) transferred to the recoil electron depends on the scattering angle and can vary from zero to a large fraction. Figure 2.2 illustrates this process.

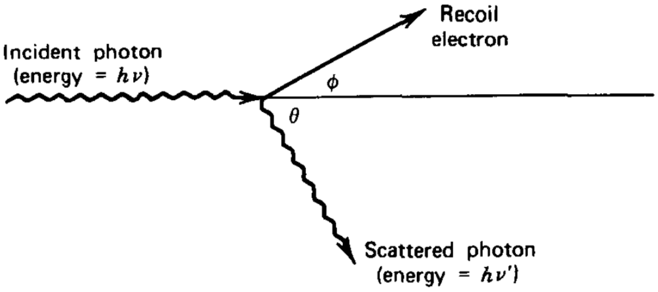

Figure 2.2: Compton scattering. Image from [22].

Compton scattering is the predominant gamma-ray interaction mechanism with matter for typical radioisotope sources energies. The probability of Compton scattering per atom of the absorber is proportionally related with the number of scattering targets, i.e. available electrons, and therefore increases linearly with Z. In addition, it generally falls off gradually with increasing energy. The description of the angular distribution of scattered gamma rays for the differential scattering cross section $d\sigma/d\Omega$ is given by:

$$\frac{d\sigma}{d\Omega} = Zr_0^2\left(\frac{1}{1+\alpha(1-cos\theta)}\right)^2\left(\frac{1+cos^2\theta}{2}\right)\left(1+\frac{\alpha^2(1-cos\theta)^2}{(1+cos^2\theta)[1+\alpha(1-cos\theta)]}\right) \tag{2.5}$$

where $\alpha = hv/m_0c^2$ and r_0 is the classical electron radius.

Pair production

In pair production, the incident gamma-ray photon is transformed in a electron-positron pair, in the coulomb field of a nucleus which absorbs the recoil momentum. For this mechanism to happen, the gamma-ray energy has to exceed twice the electron rest-mass energy (2 x 511 keV). Pair production is only dominant for high-energy gamma rays (several MeVs). The photon energy that exceeds 1.02 MeV is carried in kinetic energy shared by the electron and the positron. There isn't a simple expression for the probability of pair production, but it depends approximately on Z^2.

In the Figure 2.3 is summarized the relative importance of the three mentioned mechanisms.

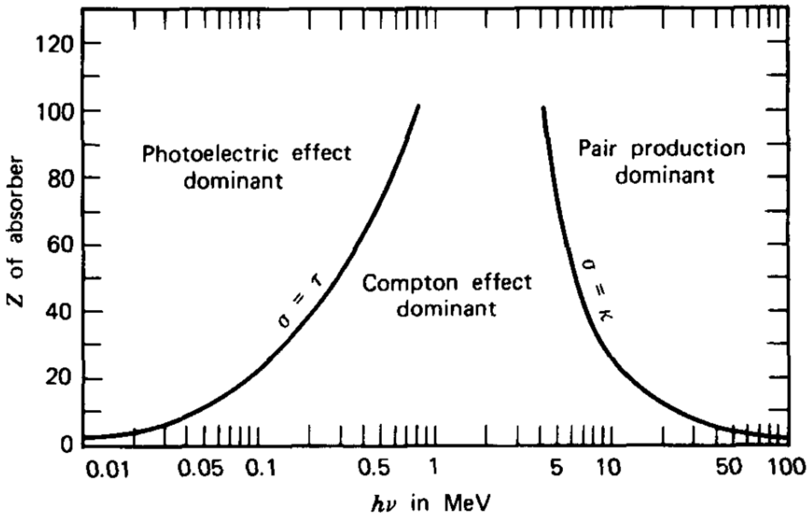

Figure 2.3: The relative importance of the three major types of gamma-ray interaction as a function of incident photons energy. The lines show the values of Z and hv for which the probability per unit path length of two neighboring effects are just equal. τ denotes this probability for photoelectric effect, θ is the same for Compton effect and κ refers to pair production. Image from [17].

Attenuation coefficient

Considering an incident photon flux in a target material, a fraction of the photons is removed from the beam by photoelectric absorption, Compton scattering and (above 1.02 MeV) pair production. Other photons are transmitted through the material. The interaction cross section σ, represents the probability that a photon will undergo one of the three interaction processes. It can be calculated as follows:

$$\sigma = \phi_{photo} + Z\sigma_c + \tau_{pair} \tag{2.6}$$

where ϕ_{photo}, σ_c and τ_{pair} are the cross sections for photoelectric absorption, Compton scattering and pair production. The values of these cross sections, depend on the radiation energy as well as on the material. For typical radioisotope sources energies, Compton scattering is the major attenuation process.

The fraction of the incident energy which is absorbed in the material per unit length is called **total absorption coefficient** λ and it's the inverse of the mean free path of the photon (the attenuation length). n and σ are related as follows:

$$\lambda = N\sigma \tag{2.7}$$

where N is the density of atoms. Having an incident intensity I, the transmitted intensity fraction I_0 for a travelled distance x the photons is given by:

$$\frac{I}{I_0} = e^{-\lambda x} \tag{2.8}$$

2.4 Scintillation phenomenon in inorganic crystals

Scintillation is a process where a flash of light is produced in a material by the passage of a particle. In inorganic crystals, the scintillation mechanism is characteristic of their the electronic band structure, which is presented in Figure 2.4.

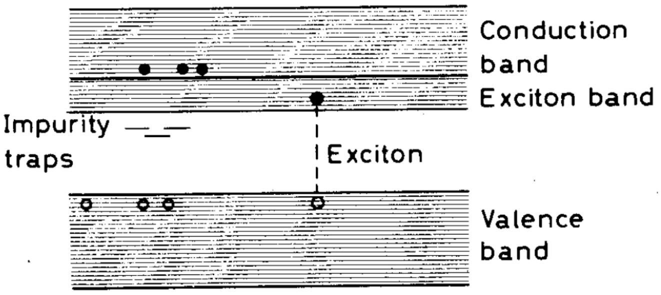

Figure 2.4: Energy band structure of an activated crystalline scintillator. Image from [22].

When a particle hits the crystal it excites a high number of electrons in a chain, from the previously mentioned mechanisms (Section 2.1 to 2.3). This excitations are from the valence band either to the conduction band, or to the exciton band, which is located right below the conduction band. In the first situation, a free electron and a free hole are created. In its turn, in the second situation, the electron and hole remain bound together as an exciton pair, moving freely through the crystal. The return of an electron to the valence band with the emission of a photon is called scintillation.

If the crystal contains impurity atoms, called activators or dopants, special sites in the crystal lattice are created, where the original energy band structure is modified. These sites are called luminescence or recombination centers and allow new energy states to appear within the forbidden gap. If an exciton pair encounters a luminescence center, they can ionize the impurity atom. If a subsequent electron arrives, it can de-excite back to the valence band with less energy than the original transition. As a result, a visible photon can be emitted, causing the scintillation phenomenon. The presence of dopants, as cerium (Ce) in this work, allows crystals transparency to their own scintillation emission.

The number of exciton pairs produced is proportional to the energy deposited in the crystal by the incident particle. As a result, the number of photons produced varies also near linearly with the deposited energy, generating a light pulse whose intensity increases with the absorbed energy. In our case, this light pulse is collected by a PIN photodiode which converts the irradiance in a proportional voltage signal.

2.5 PIN Photodiode Operation

When the scintillator crystal emits optical photons, they have to be converted into an electric signal by a readout system. The photodiode is the readout system chosen for REPE.

A PIN photodiode is a semiconductor material constituted by the N layer having an abundance of holes (positive), the P layer having an abundance of electrons (negative) and an highly resistive intrinsic layer in between. This intrinsic (depletion) layer is a undopped (pure) semiconductor called i-type semiconductor.

Thus, there is a built-in potential difference and an electric field across the depletion region. The wide intrinsic region is in contrast to PN photodiodes. The Figure 2.5 illustrates PIN photodiode structure.

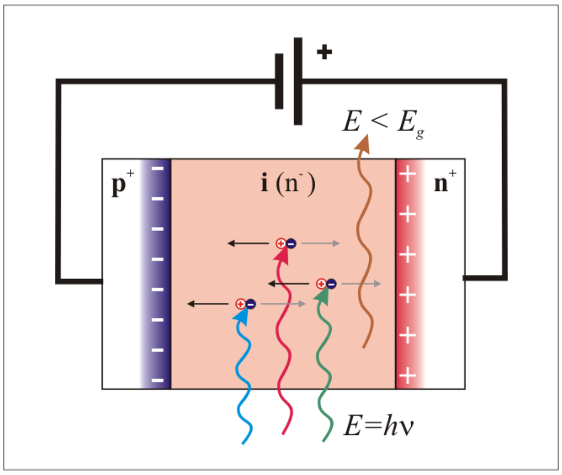

Figure 2.5: PIN photodiode scheme. Image from [42].

In semiconductors, the energy difference between the top of the valence band and the bottom of the conduction band is called gap energy (E_g), where no electronic states are allowed. E_g corresponds to the energy required to promote a valence electron bound to an atom to become a conduction electron, which is free to move within the crystal lattice and serve as a charge carrier to conduct electric current.

When a photon with energy (E) greater than semiconductor's gap energy (E_g) strikes the diode, it creates an electron–hole pair. If the photon absorption occurs in the junction's depletion region, or one diffusion length away from it, these carriers are swept from the junction by the built-in electric field of the depletion region. Thus holes move toward the anode (P region), and electrons toward the cathode (N region), and a photocurrent is produced.

The PIN photodiode operates with an applied reverse bias voltage and, to first order, the photocurrent is linearly proportional to the absorbed power. The responsivity of a photodiode is the photocurrent produced by absorbed optical power, and depends on the photodiode and on the wavelength of the incident photons. For wavelengths higher than $\lambda_g = \frac{hc}{E_g}$, responsivity drops quickly, as the energy is not enough to generate a carrier. On the other hand, for too short wavelengths, the photons pass through the device and are not absorbed. In this zone, responsivity is proportional to wavelength [13]. The result is a general wavelength response as illustrated in Figure 2.6.

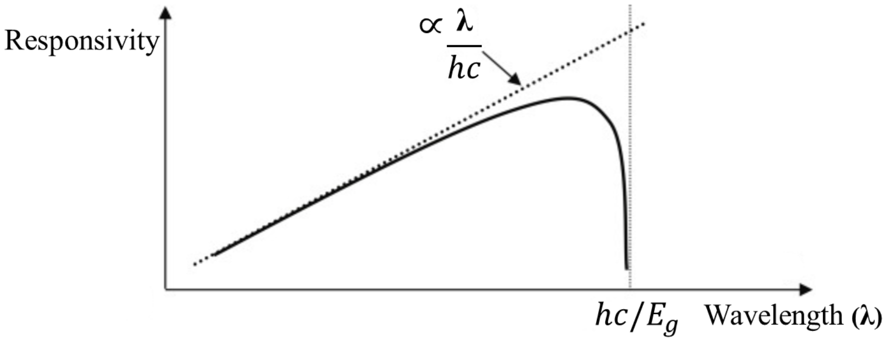

Figure 2.6: Photodiode responsivity versus wavelength.

2.6 Scintillator detector performance parameters

In this section, the main performance parameters of scintillating detectors will be briefly presented. The knowledge of these parameters allow the choice of a scintillator suitable for the purpose of the radiation detector. More details on these parameters can be found at Leo [22].

Light Yield

One of the main parameters of a scintillating crystal used as a radiation detector is the Light Yield (photons/MeV) which describes on average how many photons are produced by the medium for each absorbed MeV. Light yield depends on crystal's molecular structure, dopant type and quantity and defects in the crystals.

Decay Time

The decay time (ns) is characteristic of the particular scintillation material and determines the rate at which the light is emitted following the excitation by an incident particle. Decay time is related to the time needed for a charged pair to decay from it's excitation state. Decay time dictates how fast a detector is, as it's associated with the duration of the light pulse emitted when a particle is detected. It should be considered, for example, in order to prevent the duration of a pulse of light emitted being longer than the interval between the arrival of particles (signal pile up).

Crystal light output

Let's consider a radiation detector, composed by a scintillator crystal, and a PIN photodiode readout on one of its face, as it's the one used for this work. In order to achieve a high light output to the photodiode, it's necessary to guarantee good performance in all detection chain: (1) the absorption of incident particles by the crystal, (2) light yield (3) scintillation photons transport until they reach the output face of the crystal and (4) the light transfer from the output face of crystal until the active zone of photodiode.

The performance of each of these steps depends on the following:

- (1): The absorption depends on the surface characteristics of the crystals. Clean and low reflective surfaces present more absorption.
- (2): Light yield depends on crystal's structure
- (3): Light transport losses are consequence of the absorption, scattering and reflections in the crystal bulk and enveloping materials.
- (4): Light transfer depends on reflection losses due to mismatch of the refractive indexes of scintillator and photodiode. This can be Fresnel losses and internal reflections, which will be approached in Section 2.7.

The losses in all of these steps must be minimized as much as possible in order to achieve maximum light output and signal to noise ratio. The present work focuses on a choice of a crystal with high absorption and light yield (step (1) and (2)), choice of wrapping for light transport improvement (step (3)) and choice of optical matching medium for a good light transfer (step (4)) to the photodiode.

Photodiode quantum efficiency and photosensitivity

The photodiode quantum efficiency measures the number of photoelectrons produced divided by the number of incident photons. The amount of electric current produced by these photoelectrons for a given absorbed wavelength is called "Photosensitivity". Photosensitivity presents negligible values outside the wavelenght input range of the photodiode. This spectral response in usually specified by photodiode manufacturer. Therefore, it's important to guarantee that the scintillation photons energies match the input range of the photodiode.

Energy resolution

Another important parameter of a detector is its energy resolution, which is related to the statistical fluctuations of the light output. Energy resolution of a scintillator detector suffers contributions from the crystal intrisic resolution, photodiode resolution and amplification electronic system resolution. The total energy resolution of a photopeak is characterized by the full-width half maximum (FWHM or ΔE) of the peak divided by the mean value and can be written as:

$$(\Delta E/E)^2 = (\delta_{int})^2 + (\delta_p)^2 + (\delta_{st})^2 \tag{2.9}$$

Where δ_{int} is the intrinsic energy resolution of the crystal, δ_p is the light transfer resolution and (δ_{st}) is the statistical contribution defined by the fluctuations associated to the number of detected photon by the photodiode and by the detector noise.

With respect to crystal intrinsic resolution, light yield non-proportionality is one of the main causes for energy resolution deterioration [36]. A brief discussion on intrinsic non-proportionality will be presented next.

Light transfer is related to the losses on light collection and to matching between the crystal emission spectrum and sensitivity of photodiode. A decrease of losses in light transport and light transfer contributes to an enhancement of light transfer resolution and consequently of detector performance enhancement. This is one of the main focuses of the present work.

Intrinsic non-proportionality

As discussed in the Section 2.4, the emission of photons from a scintillator is a result of high energy excited electrons and holes, created by the incident radiation. These electrons and holes lose energy producing high density excited electron-hole pairs. Next, some of these excitons recombine radiatively and generate visible photons. If they recombine only radiatively, a proportional scintillator response is expected. However nonlinear nonradiative processes of losing energy between electron-hole excitations (quenching) are involved and the light yield turns a complicated function [5]. This phenomenon is known as non-proportionality in the scintillator response and it's one of the main reasons of intrinsic energy resolution deterioration of a scintillator crystal. Although scintillators have been studied for decades, the causes of non-proportionality are not yet clearly understood.

One explanation for non-proportionality can be based on the fact that the denser is the local ionization, the more chances there are for a free electron to recombine nonradiatively. This phenomenon is known as the Birks effect [4]. The Birks effect can be ignored for electrons and photons since their linear energy transfer is relatively low, but it significantly affects the detection of heavier particles such as protons and ions. According to Birks:

$$dL/dx = \frac{S|dE/dx|}{1 + kB|dE/dx|} \tag{2.10}$$

where

L: light output

S: a normalization constant

E: the particle energy

kB: a measure of the Birks effect influence on the light output

It's known that $-dE/dx$ decreases with E meaning Birks effect becomes negligible for higher energies. In other words, for large incident energy E the light output is approximately linear.

Sensitivity and noise

Sensitivity (D) quantifies the minimum amount of radiation that the detector can measure with a given uncertainty. The sensitivity of a system depends heavily on the noise level, i.e, statistical fluctuations that add to the signal.

In a scintillation detector, with a bandwidth Δf, constituted by the scintillator crystal, photodiode and electric readout system, the total current noise is a sum of 3 main contributions: radiation shot noise I_{sh}, dark current noise I_{dc} and readout noise I_{rd}, governed by Poisson statistics. The total current noise is given by:

$$I_{noise} = \sqrt{I_{sh}^2 + I_{dc}^2 + I_{rd}^2} \tag{2.11}$$

Radiation shot noise results from the inherent statistical variation at incident photon detection on the photodiode. If I_p is the signal current contribution of each electron, with a charge e, then shot noise is calculated as follows:

$$I_{sh} = \sqrt{2 \times e \times I_p \times \Delta f} \tag{2.12}$$

where e is the electron charge.

Dark noise arises from statistical variation in the current produced by electrons thermally generated within the silicon structure of the photodiode I_{dark}, which is independent of photon-induced signal, but highly dependent on device temperature. Dark noise is given by:

$$I_{dc} = \sqrt{2 \times e \times I_{dark} \times \Delta f} \tag{2.13}$$

Readout noise is a combination of system noise components inherent to the process of converting photodiode charge carriers into a voltage signal for quantification, and the subsequent processing and analogue-to-digital (A/D) conversion. One main type of read noise is Johnson–Nyquist noise (thermal noise) (I_t) is the electronic noise generated by the thermal agitation of the charge carriers (usually the electrons) inside an electrical conductor at equilibrium, which happens regardless of any applied voltage. Thermal noise is proportional to temperature and is approximately white, meaning that the power spectral density is nearly constant throughout the frequency spectrum. Other important electronic noise is the Flicker noise, which has a $1/f$ power spectral density, being present in low frequencies (pink noise). It's believed that Flicker noise is caused by charge carriers that are randomly trapped and released between the interfaces of two materials. This phenomenon typically occurs in semiconductors that are used in the amplifiers of the instrument to record electrical signals. If k is Boltzmann's constant, T is the absolute temperature and R is the resistance value, then thermal noise current inside a electric conductor is:

$$I_t = \sqrt{\frac{4 \times k \times T \times \Delta f}{R}} \tag{2.14}$$

Depending on the crystal and on the conditions, a background radiation can also be present in the measured signal, which is related to luminous background sources or intrinsic radioactivity of the scintillator. The next subsections contains more details on this.

Other characteristics

There are other characteristics that influence the whole detector efficiency and must be taken into account to make a suitable choice of a scintillator crystal. These characteristics are intrinsic radioactivity, radiation resistance, hygroscopicity and temperature dependence.

Some scintillators present **intrinsic radioactivity** as they present an element which is radioactive. If at the first sight, intrinsic radioactivity in scintillator crystals can seem to be a disadvantage as it adds radiation to the interest signal, it can also be an advantage is space applications. Intrinsic radioactivity is an easy way to perform energy calibration on scintillator detectors, with no external radioactive source being required.

Radiation resistance is related to the longevity and reliability of a detector. It is related to the change in emitted light and transmittance after the material is exposed to high radiation [15].

Another characteristic related to the longevity of a detector is **hygroscopicity**, which is the ability to easily absorb moisture from ambient atmosphere. Hygroscopic materials deteriorate and change their physical form, degrading their scintillating properties, due to the interaction with that moisture. A common solution to this problem has been the use of protective packaging [46].

In general, the response of scintillators is **temperature dependent**, since the light output of scintillation crystals and the decay time depend on temperature [35]. This is because the number of radioactive excited states depends on the temperature. At higher temperatures, the decay time starts to decrease attributed to the thermal detachment of holes of acceptor atoms [7].

2.7 Critical angle, Reflectance and Transmittance

For an incident photon flux with an angle θ_i from the perpendicular on the interface of two media of different refractive indexes, a fraction R is reflected with the same angle θ_i and a fraction (1-R) is refracted with an angle θ_t. Snell's law describes this light change of direction as follows:

$$n_i sin\theta_i = n_t sin\theta_t \tag{2.15}$$

where n_i and n_t are the refractive index of the initial and final media of the light path, respectively. When n_t is smaller than n_i, from a certain angle of incidence (critical angle θ_c), the wave is totally reflected, remaining in the same medium of incidence. This phenomenon is called total internal reflection, and the critical angle is given by:

$$sin\theta_c = n_i/n_t \tag{2.16}$$

On the other hand, to obtain the ratio between the incident power (or flux) and the reflected power or transmitted power, reflectance (R) or transmittance (T) are used. Light polarized with electric field paralell to the plane-of-incidence has different transmittance and reflectance than light polarized in perpendicular. In the case presented here, the light is not polarized so that the transmittance and reflectances are the average of parallel ($\|$) and perpendicular ($\perp$) cases. Transmittance and reflectance were obtained using Fresnel equations, and are presented in the following equations:

$$T_\perp = \frac{n_t cos\theta_t}{n_i cos\theta_i}\left(\frac{2n_i cos\theta_i}{n_i cos\theta_i + n_t cos\theta_t}\right)^2 \tag{2.17}$$

$$T_\| = \frac{n_t cos\theta_t}{n_i cos\theta_i}\left(\frac{2n_i cos\theta_i}{n_i cos\theta_t + n_t cos\theta_i}\right)^2 \tag{2.18}$$

Using the Snell law, transmittance can be obtain by:

$$T_{\perp} = \frac{n_t\sqrt{1-(n_i/n_t sin\theta_i)^2}}{n_i cos\theta_i}\left(\frac{2n_i cos\theta_i}{n_i cos\theta_i + n_t\sqrt{1-(n_i/n_t sin\theta_i)^2}}\right)^2 \tag{2.19}$$

$$T_{\parallel} = \frac{n_t\sqrt{1-(n_i/n_t sin\theta_i)^2}}{n_i cos\theta_i}\left(\frac{2n_i cos\theta_i}{n_t cos\theta_i + n_i\sqrt{1-(n_i sin\theta_i/n_t)^2}}\right)^2 \tag{2.20}$$

$$T = \frac{1}{2}(T_{\perp} + T_{\parallel}) \tag{2.21}$$

$$R = 1 - T \tag{2.22}$$

The graphic of transmittance and reflectance vs incident angle is presented in the Figures 2.7 and 2.8, for the case of lower to higher refractive index light propagation and higher to lower refractive index light propagation, respectively.

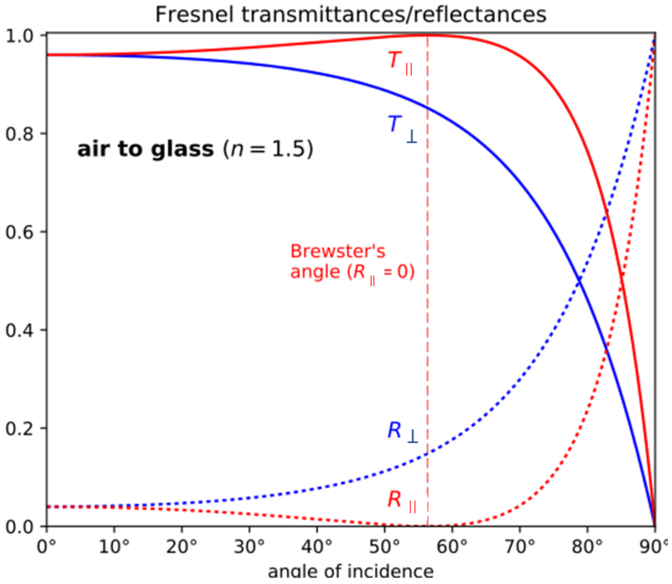

Figure 2.7: Transmittance and reflectance in light transmission from air (lower refractive index) to glass. Image from [41].

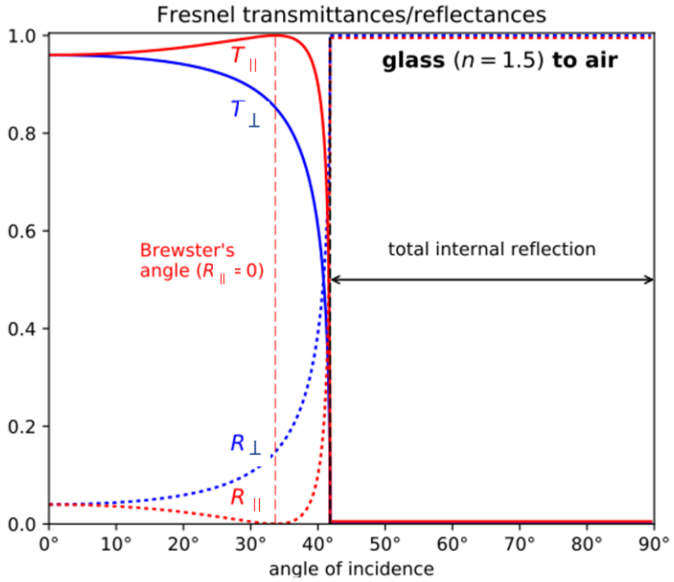

Figure 2.8: Transmittance and reflectance in light transmission from glass (higher refractive index) to air. Image from [41].

Chapter 3

State of the art

3.1 Van Allen Radiation Belts

Discovery

In 1957, the Soviet Union launched their first two satellites, Sputnik 1 and Sputnik 2. Sputnik 1 had no scientific instruments on board and Sputnik 2 carried Laika dog, the first living animal orbiting the Earth and two radiation detectors (Geiger-Muller tubes). These detectors registered unexpected fluctuation on radiation data, but no conclusions were drawn about that. Beginning the space race against the Soviet Union, the USA launched, in 1958, their first satellite, Explorer 1, under the direction of Dr. James Van Allen. Explorer I contained a Geiger–Müller tube on board to detect cosmic rays. However, this detector was saturated most of the time. In the following months, two more USA satellite missions (Explorer III and Pioneer III) confirmed that Dr. James Van Allen and his team were detecting the radiation belts with energetic charged particles that were located around the planet Earth. This radiation belts were called Van Allen Radiation Belts.

It was quickly realized that Van Allen radiation belts influenced the operation and orbit of satellites, leading to numerous malfunctions, in addition to being a risk to the health of astronauts. The study of these radiation belts has become a focal point in spacecraft engineering, military and scientific teams. In addiction, the fundamental physics discoveries of the Van Allen radiation belts contribute to the understanding of the dynamics of energetic charged particles on other magnetized planets [23].

Numerous missions were carried out in the following years with the aim of collecting data for a detailed understanding of the Van Allen radiation belts. NASA's Van Allen Probes were two of those satellites, active in orbit between 2012 and 2019 that contributed in a huge way to the knowledge that we have today about this radiation belt. However, it was also perceived that the level of complexity of the physical processes of the Van Allen radiation belts is enormous and that there are still many details to unravel.

Brief description

The Van Allen radiation belts consists of charged particles, mainly protons and electrons, but also other nuclei such as alpha particles and some ions, trapped in the Earth's magnetosphere. The origin of these particles is mainly solar wind and the Earth's atmosphere [18]. There are two Van Allen radiation belts, an inner belt and a dynamic outer belt (see Figure 3.1). Other belts can be temporarily observed between the inner and the outer belts as a result of solar energetic particles being trapped inside the magnetosphere.

The inner belt is smaller and more stable. It consists of energetic protons, ions and electrons and is located at equatorial distances of about 1.1 to 2 R_E ($R_E \approx 6370$ km is the radius of Earth).

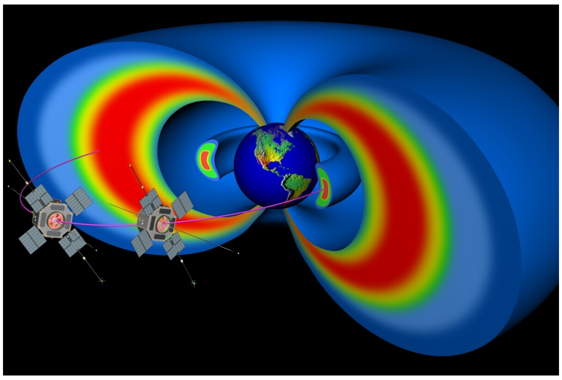

Figure 3.1: Inner and outer Van Allen radiation belts and Van Allen Probes A and B orbiting through the two belts. Image from [27].

The inner belt has the most intense radiation of the Van Allen belt. Hundreds of mega-electron volt (MeV) protons and up to about 1 MeV electrons can be found in this zone. The protons from the inner zone belt are originated by Cosmic Ray Albedo Neutron Decay (CRAND), solar flares and coronal mass ejections. CRAND consists of decay of neutrons produced by cosmic rays scattering off the atmosphere.

The outer belt is much larger, located from about 3 $\mathrm{R_E}$ to $7-10$ $\mathrm{R_E}$ and centered at 19000 km from Earth. The outer belt contains electrons with energies from tens of keV to several MeV, mostly ultrarelativistic electrons. This zone is more unstable, with constant change of composition and particle fluxes and is very sensitive to variations in magnetic field. Solar wind is the main source of electrons in the outer zone.

Between the two belts there is the so-called Slot region with low radiation flux due to the loss by pitch angle scattering to the atmosphere by circularly polarized electromagnetic waves called Electromagnetic Ion Cyclotron (EMIC) and whistler mode waves [23].

The flux of protons and electrons in the Van Allen radiation belts varies with energy, type of particle, L (parameter that describes the distance from Earth's magnetic equatorial plane in $\mathrm{R_E}$) and solar and magnetospheric activity. In the Figure 3.2 are presented the >10 MeV proton and >1 MeV electron flux distribution obtained by the NASA AP-8 MAX model [34] and AE-8 MAX model [40] respectively, during solar maximum (the regular period of greatest solar activity during the Sun's 11-year solar cycle) .

Particle dynamics

Trapped electrons and protons, within the Van Allen radiation belts, perform three nearly periodic motions due the interaction with the geomagnetic field. They rotate around a magnetic field line, undergo bounce−motion between hemispheres reflected in the strong magnetic field, and drift perpendicularly to the magnetic field, to the west (protons) or east (electron) around the Earth (see Figure 3.3).

Although these three motions are well described by classical physics, the particle acceleration processes in the radiation belts are not fully described by these motions. A conservation of adiabatic invariants does not explain as strong particle acceleration as it is observed during geomagnetic activity. That is why wave-particle interactions (which break the conservation of these invariants) are thought to be important for the intensification (and decay) of the radiation belts.

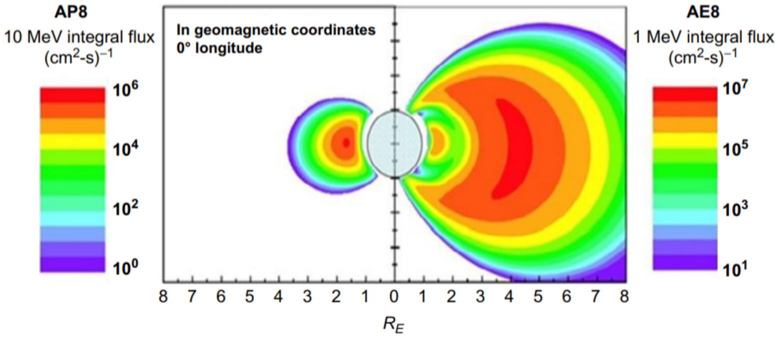

Figure 3.2: Integral flux ($cm^2\ s^{-1}$) of protons (>10 MeV) and electrons (>1 MeV) as a function of altitude (where 1 R_E = 6371 km) in Earth orbit at 0° longitude, using the AP8/AE8 models at solar maximum. Generated by using the AE8/AP8 models in SPENVIS [12]. The mapping is done in magnetic coordinates given here in earth radii. Image from [20].

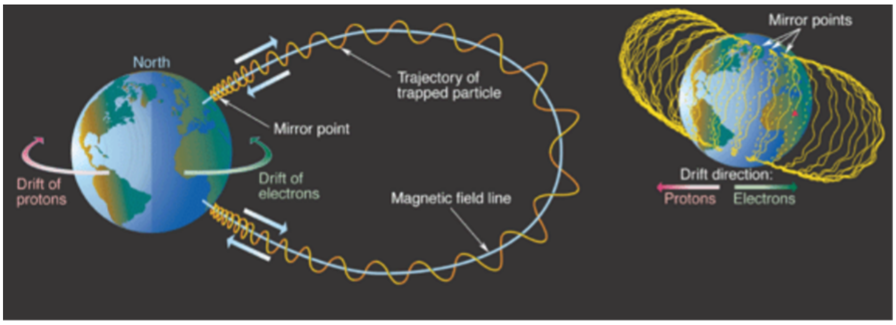

Figure 3.3: Three quasi-periodic motions of charged particles within Van Allen radiation belt. Image from [2].

One of the scientific challenges of recent years lies in realizing which acceleration and transport processes leads the increase in particle energy towards relativistic and ultrarelativistic energies. Understand the particle loss mechanisms is equally important [18].

Transport and acceleration

It is believed that there are two main particle acceleration mechanisms: radial transport and local acceleration. Distinguishing between the two processes and knowing which is dominant has been historically complex and it is a topic under scientific debate.

Radial diffusion transports distant particles towards the earth, accelerating the particles as they move from a weaker to a stronger magnetic field. This mechanism is thought to be consequence of ultra low-frequency (ULF) electromagnetic fluctuations in the magnetic field. It's believed that these waves can have their origin in interplanetary shocks from the sun (driven by coronal mass ejections (CMEs)) [23].

Local acceleration includes mechanisms that accelerate particles at the center of radiation belts through interactions with circularly polarized electromagnetic waves. These phenomena change the pitch angle in their rotation around magnetic field line, and energize the particles. These processes are caused by waves generated by anisotropies of the plasma particle, called chorus Whistler-mode waves and EMIC (electromagnetic ion cyclotron) waves.

These two types of acceleration mechanisms, individually, present different phase-space density (PSD) evolution with L or time (see Figure 3.4). This is one of the ways in which measurements of fluxes and energies of particles in the radiation belt allow the distinction and identification of physical processes occurring.

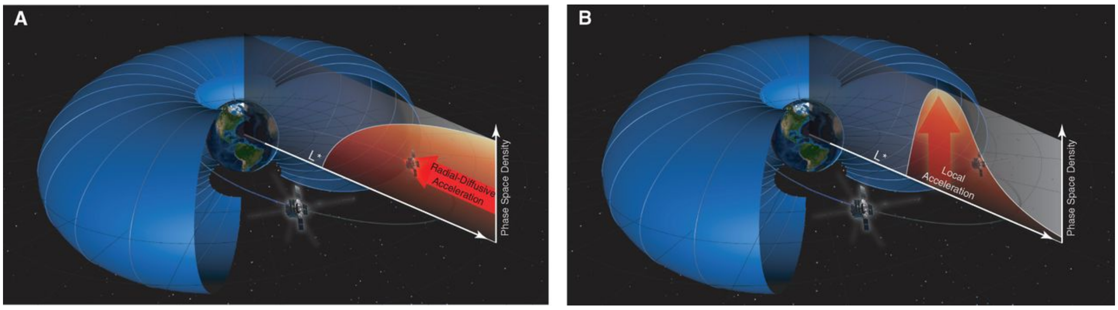

Figure 3.4: PSD evolution in a radial diffusive acceleration (A) and local acceleration (B). Image from [32].

A theoretical description of the evolution of PSD due to these mechanisms can be done through the reduced Fokker-Plank equation or modified Fokker-Plank equation as the mechanism is radial diffusion or local acceleration respectively. Although Fokker-Planck equation describes PSD evolution, it contains diffusion coefficients that can be difficult to obtain. In addition, a slightly distorted dipole field geometry leads to complications. Obtaining the diffusion coefficient empirically is not straightforward either, it is limited by the observations performed and sometimes different works lead to contradictory results. With all of these challenges, there is no universal method to describe these particles motion numerically or analytically, for all energies and scales

Losses

Regarding the loss mechanisms of particles from the radiation belt, two main processes are identified, the loss to atmosphere and the loss to magnetopause.

The loss of particles to the atmosphere is called precipitation and it occurs when particles pitch angle (see Figure. 3.5) enter the so-called loss cone. When this condition is satisfied, when particles reach the poles, they are transmitted to the atmosphere instead of being reflected to the other pole in their bounce movement between these magnetic mirror points.

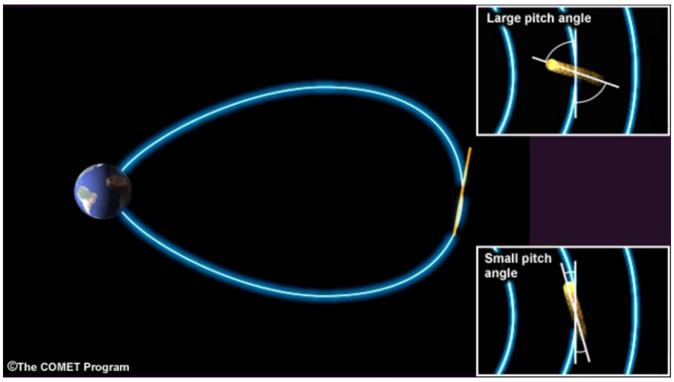

Figure 3.5: Pitch angle. Image from [43].

The EMIC and Whistler-mode chorus waves are the main responsible for, in their interaction with the particles, shifting their pitch angle to the loss cone. Thus these waves have a dual role in the interaction with the Van Allen belt particles, they can both accelerate and remove them from the belt.

Another mechanism that causes loss of particles from the radiation belt is the compression of the magnetopause by the solar winds. Here, trapped electrons are lost to the magnetopause by a number of consequent mechanisms.

In the same way as with acceleration mechanisms, it is also possible to distinguish between different loss mechanisms in the temporal evolution of the PSD .

Outstanding challenges and REPE contributions

Despite significant advances that have been made in understanding particle dynamics across the Van Allen radiation belts, there are still many details to explore. Global radiation belt models need find ways, to incorporate the effect of realistic waves in order to describe, predict and relate phenomena in every time and dimension scales and range of energies. Another challenge is to couple the physical models of the radiation belt to solar and geospatial models (e.g., solar wind, tail plasmasheet, plasmasphere, and ionosphere) [23].

Measuring energy spectrum of relativistic protons and electrons in the most intense radiation zone of Van Allen radiation belt, REPE aims to contribute to answering questions such as:

- *Which mechanisms contribute to the precipitation of energetic charged particles to the atmosphere?*
- *What is the role of ULF and EMIC waves in accelerating, transporting, and scattering electrons in the Van Allen radiation belts, as a function of solar wind driving and magnetospheric activity?*
- *How do ULF and EMIC waves and turbulence transmit within the inner magnetosphere?*

3.2 High energy detectors

In astrophysics, high energy detection has multiple applications, such as the study of the origin of cosmic rays, the laws of physics around neutron stars and black holes and development of cosmology and fundamental physics. Furthermore, also the relativistic and ultrarelativistic electrons and protons on the Van Allen radiation belt have measured high energies from hundreds of keV to dozens of MeV to electrons, or hundreds of MeV to protons.

The main types of high energy detectors are gaseous ionization detectors, semiconductor detectors, Cherenkov detectors and scintillation detectors [17]. Scintillation detectors are the focus of the present work and, as such, will be discussed in more detail.

Gaseous ionization detectors

Gaseous ionization detectors working principle is based on the ionising effect of radiation when interacting with molecules of a gas-filled sensor. When an incident particle has enough energy to ionize a gas atom or molecule, the resulting electrons and ions cause a current flow which can be measured. There are three basic types of gaseous ionization detectors: ionization chambers, proportional counters, and Geiger–Muller tubes [17].

In ionization chambers, the voltage is not high enough to produce gas amplification (secondary ionization). A Geiger-Muller detector (unlike proportional counters) operates on high voltage and ionization avalanche mode. This way, the output is not proportional to the energy of incident particle. It's used for radiation intensity measurement. Geiger-Muller detectors were the detector types aboard on the satellites that discovered Van Allen Radiation Belt: Explorer I,III and Pioneer III, mentioned in the Section 3.1 ”Van Allen Radiation Belts”.

Semiconductor detectors

Semiconductor detectors are commonly used when good energy resolution is intended. In this type of detectors, the fundamental information carriers are electron-hole pairs, which are produced along the path taken by the charged particle (primary or secondary) through the detector. By applying an external voltage, electron-hole pairs are collected and the detection signal is formed. This is the operation principle of photodiodes, which are explored in more detail in the Section 2.5 ”PIN Photodiode Operation”.

Cherenkov detectors

Cherenkov is a speed-dependent light output detector. It is based on the emission and detection of Cherenkov radiation, which is emitted when a charged particle moves through a dielectric medium faster than the phase velocity of light in that medium. Cherenkov radiation is visible light or UV photons and it’s intensity is proportional to the charged particle path length in the medium.

Therefore, Cherenkov counters are composed of two main elements: a dielectric radiator through which the charged particle passes, and an optical photodetector to measure the resultant radiation (e.g. a photomultiplier tube or photodiode).

Scintillator Detectors

Today, several scintillator crystals are used for different applications. In astrophysics, scintillation detectors are used to detect all types of radiation, including X-rays, γ-rays, protons, electrons, neutrons, α-particles, and neutrinos [1].

The main reason why a scintillator detector was chosen to constitute REPE instrument is that it allows solutions of very small size associated with high stopping power, good detection efficiency and sensitivity to high energies. The fact that it allows readout solutions with reduced power consumption, noise and dimensions, such as silicon photodiodes, was another contribution for this choice.

Briefly summarizing scintillation process, it occurs when a detector material is excited by absorbing photons or particles and in the process of de-excitation emits photons in the visible or near-visible range. The number of emitted photons is proportional to the energy of the absorbed particle [19]. For more details consult the Section 2.4 ”Scintillation phenomenon in inorganic crystals”. The light pulses generated are collected by a photodetector readout (see Figure 3.6) which produces a current proportional to the deposited energy in the crystal by the incident particle. A deeper discussion on this photodetectors are found in Section 3.3 ”Scintillators readout: optical photodetectors”.

The disadvantage of scintillator crystal detectors is that, in general, they have a limited spectral performance [10] and often must be combined with another type of detector.

Types of scintillators

There are two types of scintillators, organic and inorganic. Organic scintillators such as stilbene, anthracene and liquid scintillators are made up of organic compounds. This type of scintillator is fast (small decay time) and has an excellent pulse shape discrimination capability that favors the distinction between incident particle types. However, they have a low light yield.

In the other hand, inorganic scintillators are typically ionic solids composed of high density crystals and high atomic number and, in turn, greater detection efficiency (stopping power) compared to organic ones.

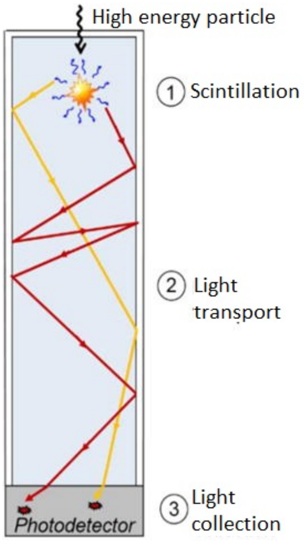

Figure 3.6: Scintillator detector and two emitted photons paths (red and yellow) until the photodetector. Image adapted from [33]

Furthermore, the melting temperature for inorganic scintillators is generally higher than that for organic scintillators. For this reason, inorganic scintillators are more resistant to high temperatures than organic ones [16].

The crystals chosen as candidates to constitute the scintillation detector of the REPE are inorganic crystals, and it is on these that the present study will focus.

Main inorganic scintillator crystals

Among the longest-used inorganic scintillators are crystals of thallium doped sodium iodide (NaI:Tl), thallium doped cesium iodide (CsI:Tl) and bismuth germanate or BGO ($Bi_4Ge_3O_{12}$). These crystals are relatively efficient but have long decay times (>200 ns) because their electron transitions are spin forbidden [6]. In addition NaI:Tl is highly hygroscopic.

In recent years, modern inorganic scintilators have emerged, which have been replacing the previous ones, with the best combination of speed and efficiency which are cerium-doped. Gadolinium Aluminium Gallium Garnet ($Gd_3Al_2Ga_3O_{12}$) doped with Ce (GAGG:Ce), Lanthanum Bromide Ce doped ($LaBr_3$:Ce) and Cerium Bromide ($CeBr_3$) are an example of those crystals. In addition to the above, there are also two commercially produced cerium-doped rare earth silicates: Gadolinium Orthosilicate or GSO (Gd_2SiO_5) and Lutetium-yttrium oxyorthosilicate or LYSO systems ($Lu_{1-x}Y_xSi_2O_5$). These modern crystals are priced higher on the market than older ones.

In Sibczynski et al. [37] the $LaBr_3$:Ce, $CeBr_3$ and GAGG:Ce crystals were investigated and the characteristics determined compared with those determined for the well-known and widely used CsI:Tl and NaI:Tl crystals. $LaBr_3$:Ce, $CeBr_3$ and GAGG:Ce crystals showed a better performance than the old ones, as they showed good energy resolution, short decay time and high detection efficiency for MeV gamma rays. In particular, GAGG:Ce crystal presented the highest detection efficiency among all the tested scintillator crystals.

In Seitz et al. [36] the scintillating properties of GAGG:Ce, LYSO:Ce, BGO and NaI:Tl are compared. GAGG:Ce is again the most efficient in terms of light output and decay time, followed by LYSO:Ce.

LYSO:Ce and GAGG:Ce were the inorganic scintillator crystals chosen to be studied in the present work, as candidates to constitute a radiation detector to be included in REPE telescope, which aims to measure the energy spectrum of ultrarelativistic protons and electrons of the Van Allen radiation belt.

LYSO:Ce and GAGG:Ce crystals

LYSO:Ce and GAGG:Ce meet the requirements of high stopping power, high light output, good energy resolution, fast decay time, non-hygroscopic, relatively stable in temperature compared to other commonly used ones and also present a good resistance to harsh environments.

The main properties of LYSO:Ce, GAGG:Ce, NaI:Tl and CsI:Tl are indicated in Table 3.1.

Scintillator	**LYSO:Ce**	**GAGG:Ce**	**NaI:Tl**	**CsI:Tl**
Light output [photons/MeV]	29000	50000	45000	54000
Decay Time [ns]	42	88	264	1020
Emission peak wavelength [nm]	420	520	415	550
Density [g/cm^3]	7.1	6.6	3.67	4.51
Hygroscopic	NO	NO	YES	Slightly
Z_{eff}	65	54.4	50	54
Intrinsic radioactivity	YES	NO	NO	NO
Refractive index @ emission wavelength	1.82	1.9	1.85	1.79

Table 3.1: Main characteristics of LYSO:Ce GAGG:Ce, NaI:Tl and CsI:Tl crystals [14]

3.3 Scintillators readout: optical photodetectors

When a particle with enough energy hits a scintillator crystal, it emits radiation in the visible or near-visible zone. Readout systems are usually constituted by a photodetector coupled to a crystal, to convert the light pulses in an electronic signal. A processing system that amplifies the analog signal and converts it to digital is generally applied afterwards. The most common photodetector types are photomultipliers (PMT), photodiode, avalanche photodiode (APD) and silicon photomultiplier (SiPM). Photodiodes were the chosen scintillator photodetectors to be used in REPE. For more details on photodetectors, consult Knoll [17].

PMT

The basic physical principle of operation of photomultipliers tubes (PMTs) is the photoelectric effect. As presented in Figure 3.7, the light hits on the photocathode and the electrons generated by the photoelectric effect are multiplied by a sequence of photoelectric effects in a chain of dynodes associated with high voltages between them. The electrons are collected in the anode where the output pulse signal is measured. PMT are the detector types with higher intrinsic gain.

Photodiodes

The photodiode is a semiconductor material, usually silicon, germanium or indium gallium arsenide that converts optical signals into an electric current. There two main types of photodiodes, PN and PIN photodiodes [8].

The PIN photodiode working principle was already described in Section 2.5 ”PIN Photodiode Operation”, as it was the chosen photodetector for the scintillator detector for REPE. Recalling

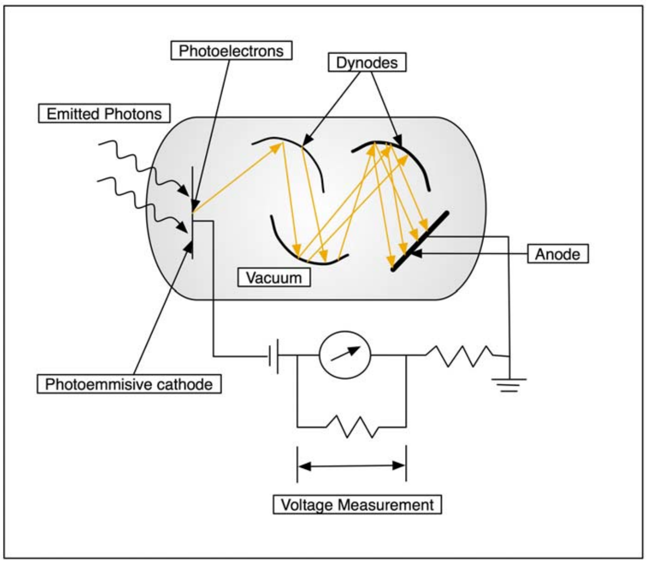

Figure 3.7: PMT. Image from [31].

that section, when a photon of sufficient energy strikes the diode, it creates an electron–hole pair that can posteriorly produce a photocurrent which is linearly proportional to the irradiance.

The PN photodiode is similar to the PIN Junction photodiode. However, instead of having an intrinsic layer, the P and N layers are together creating the depletion region.

In terms of performance, PIN photodiode have several benefit, over PN photodiodes, due to the added intrinsic layer. First, the photodiodes capacitance and the correspondent time constant are inversely proportional to the thickness. Thus, due to time constant reduction, the photodiode speed increases. However it should be noticed that the increment in depletion region thickness leads to a carriers transit time increase. On the other hand, PIN photodiodes present a capacitance reduction, and hence, a higher detection bandwidth.

Furthermore, the added layer also allows a larger volume of photon to electron-hole conversion and higher Quantum Efficiency (ratio between the number of charge carriers collected and the number of photons hitting the photoreactive surface).

APD

The diode which uses the avalanche method to provide extra performance as compared to other diodes is known as avalanche photodiode (APD). These diodes operate in high reverse bias. Avalanche breakdown occurs mainly once the photodiode is subjected to maximum reverse voltage. This voltage enhances the electric field beyond the depletion layer. This electric field is sufficiently high to enable the migrating electrons to create secondary ionization during the collection process. Thus, charge carriers will be multiplied by a variable gain, depending on their position relative to the boundaries of the multiplication region [17].

SiPM

Increasing the reverse voltage even further, above the so-called breakdown voltage, Geiger-mode avalanche operation is reached. Here holes obtain enough kinetic energy to perform also impact ionization. When operating in this regime, the silicon photodiode is often called silicon photomultiplier (SiPM) or Single-photon avalanche diode (SPAD).

In the Figure 3.8 are presented the photodiode, APD and Geiger-mode APD regimes.

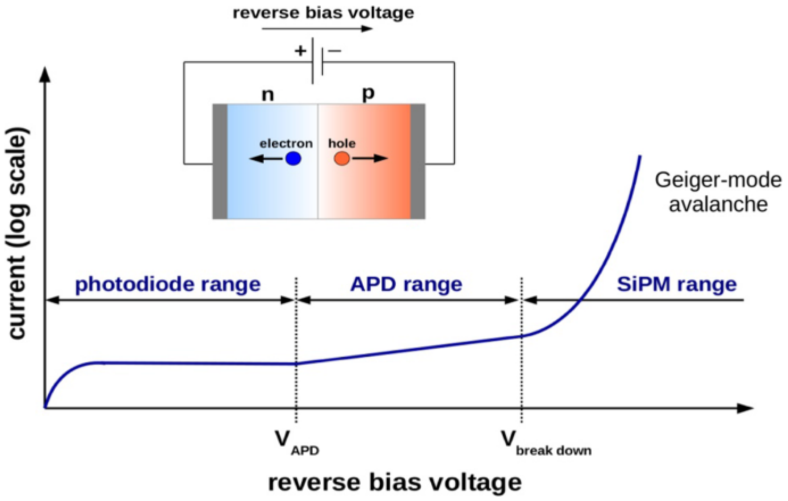

Figure 3.8: Photodiode, APD and SiPM ranges according to reverse bias voltage applied. Image from [21].

Silicon photodiodes do not have internal gain, however they have quantum efficiency greater than any other photodetector type, low power consumption, long-term stabiliy, high speed and are insensitive to magnetic fields. They also present less dark current than SiPM and ADP (despite lower signal-to-noise ratio) [29].

In this way, when quantum efficiency is the most important factor, silicon photodiodes are often the option chosen as an inorganic scintillator crystals photodetectors, associated with a low noise preamplification system. Silicon photodiodes were the inorganic scintillator photodector chosen to be studied in the present work.

Hamamatsu Photonics has a commercial series of photodiodes commonly used for readout of scintillators [44]. Hamamatsu Photonics's top competitors in photodiodes manufacturing include First Sensor and Kyosemi.

3.4 Wrapping

To prevent light from exiting the crystal by the faces that do not have a photodetector, one of the techniques used consists of wrapping or coating the crystal with a reflective/ diffusive material (see Figure 3.9).

Several studies have been made to compare the influence of various reflector materials and also in terms of the surfaces to be covered (top and side crystal faces) in the collection of light by photodetector, in several crystals. For LYSO and GAGG scintilator crystals, the most commonly used wrapping materials are teflon, aluminized myLar and TiO_2. The efficiency of the wrapping of scintillator inorganic crystals depends on the material used but also of the inorganic crystal concerned, its dimensions and the covered surfaces setup.

Auffray et al. [3] compared several wrapping materials reflectors namely: teflon, aluminium-mylar and black paper in different scenarios of covered faces. They concluded that full (top and side faces) wrapping of the scintillators, namely LYSO crystal, with a reflector, preferably teflon produces the best efficiency in the collection of light by photodetector.

In addition to wrap the crystal, polishing the surface of the scintillator crystal is also a technique that influences the light extraction. Heinrichs et al. [11] concluded that, using no

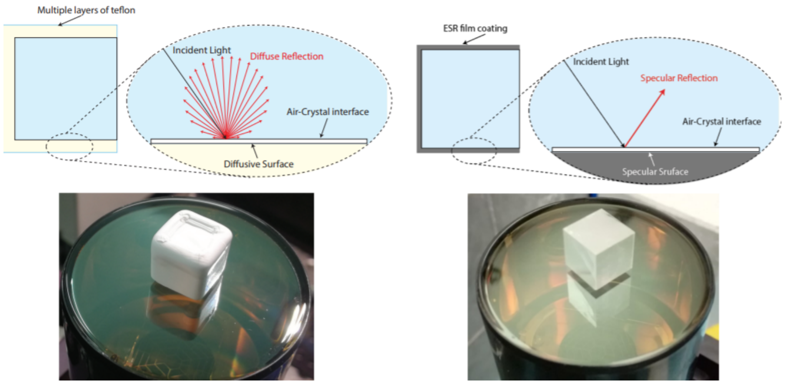

Figure 3.9: Typical scintillator wrapping examples. (Left): Teflon (diffusive) wrapping; (Right): ESR (specular) wrapping. (Top row): schematic representation; (Bottom row): Actual crystals attached to the window of a Photomultiplier Tube (PMT). Image from [9].

reflector material, the light output increased up to 551 % by mechanical polishing the surface, compared to raw material.

3.5 Crystal-photodetector transfer improvement

The high refractive index characteristic of inorganic crystals leads to internal reflections at crystal-photodetector interface. One of the most common and easy solution for this issue is to use a medium of optical coupling between the scintillator and the photodetector. In the case of inorganic scintillator crystals, a high refractive index material is desirable.

One example of a high refraction index glue in the market is the Norland Optical Adhesives NOA from Norland Products, with an refractive index from 1.315 to 1.70 [30]. NOA 169, with a refractive index of 1.69 will be used in this work. However this glue is no longer manufactured. In future works NOA 169 will be replaced by NOA 170 which presents similar properties to NOA 169, but has a refractive index of 1.70.

Chapter 4

Theoretical assessment

In this section is presented a brief theoretical approach on the light collection of radiation detectors constituted by different combinations of scintillator crystal, wrapping material, PIN photodiode type and optical matching media. This optical matching media serve to attach the crystal, wrapping and photodiode and also to match this materials refractive index.

The detector elements approached theoretically in the present chapter were next tested together experimentally, in order to confirm the theoretical expectations. The experiment results are presented on the later Chapter 6 "Results and discussion". Thus, in this chapter, the incident radiation is assumed to be gamma-rays from ^{137}Cs radioactive source with an energy of 661.7 keV, as it was the radiation source available for experiments.

In this sense, the considered options for crystals were: LYSO:Ce and GAGG:Ce. For wrapping the evaluated materials were aluminized kapton, aluminized mylar and teflon. For the readout the options were silicon intrinsic layer PIN (SiPIN) photodiodes sealed with a epoxy resin window (S3590-08 series from Hamamatsu) and SiPIN photodiode unsealed, which have the same properties of S3590-08, but doesn't contain that window (S3590-09 series from Hamamatsu). Finally for optical media we considered: general purpose silicon grease, with a refractive index of 1.55 and NOA 169 optical adhesive from AMS Technologies, with a refractive index of 1.69, as seen in Figure 5.1.

In this chapter, the setup presented in Figure 4.1 is assumed, where a cube scintillator crystal (1 x 1 x 1 cm) (yellow) is perfectly stacked by one face on a photodiode (black) and an uncollimated ^{137}Cs (red) radioactive source with isotropic emission, placed a few centimeters away from the crystal. The system is assumed to be in vacuum.

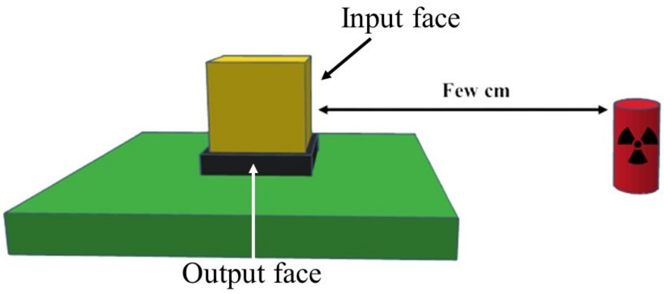

Figure 4.1: System setup assumed in theoretical predictions. Yellow: scintillator crystal (1 x 1 x 1 cm); black: photodiode, green: signal processing system and red: ^{137}Cs radioactive source with isotropic emission

4.1 Losses at crystals input and output faces

Losses at crystals entrance

Gamma-rays are emitted isotropically from the radioactive source and some of this rays reach the input face of cubic scintillator crystal. As seen in Chapter 2, gamma-rays interact less with matter than charged particles, and as such, they reach deeper distances inside scintillator crystals. In this way, the entry of gamma-rays in the crystal can be considered independent of the crystal's surface coatings or dust. In contrast, protons and electrons present smaller penetration depth and a large fraction of their energy can be deposited in crystal's surface, if not properly uncovered and clean, generating a threshold in incident energy detection. In this chapter, the crystal's input faces are considered to be without any coating or wrapping, which is the situation that leads to the least losses.

Losses at photodiode window

After a gamma ray interacts with the scintillator crystal, it produces scintillation photons that will be detected by a photodiode readout. In this crystal - photodiode interface several losses can occur. The quantity of grease/ glue used is not well determined, thus, the losses in optical media won't be approached.

One important factor related to losses in this interface is the PIN photodiode epoxy resin window. Two models are available: a sealed photodiode, which is covered by one epoxy resin window, and one unsealed photodiode, without that window. The unsealed photodiode leads to one less interface with different refractive indexes and one less medium in which photons can suffer absorption and reflection losses. Therefore, it is expected better light collection when unsealed photodiode is used.

The figure below presents a scheme of the photodiodes models considered:

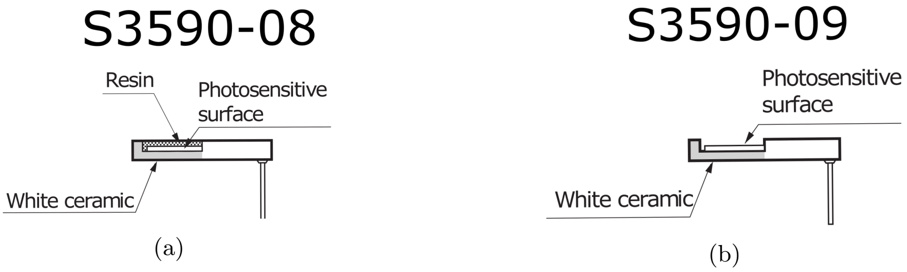

(a) (b)

Figure 4.2: Scheme of the two photodiode models to be evaluated

Another important factor that affects the losses in the interface crystal-photodiode is the photodiode sensitivity to the scintillation photons wavelength for each crystal. The photosensitivity for the spectral response range of these S3590 photodiodes is presented in the Figure 4.3.

From the graphics of Figure 4.3, it can be inferred that, for sealed photodiode (left), the curve of quantum efficiency (QE) = 100% is closest to GAGG:Ce emission wavelength response (520 nm) than for LYSO:Ce emission wavelength (420 nm). Therefore, QE is larger when sealed photodiode is coupled to GAGG:Ce. The same can be noted for unsealed photodiode (right). In addition, for 420 nm, quantum efficiency is nearest 100% in unsealed photodiode. This means, it's expected that GAGG:Ce together with unsealed photodiode lead to a larger current signal, for the same number of photons emitted by the crystals.

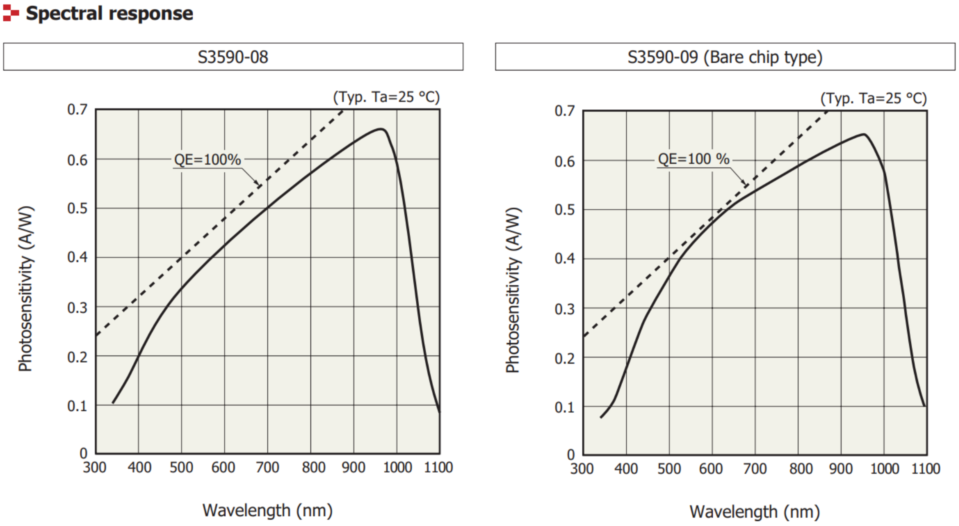

Figure 4.3: Spectral response of sealed (left) and unsealed (right) photodiodes

4.2 Losses inside the crystals

Crystals transparency

After the gamma photons enter the crystals, they will interact with the atoms through the mechanisms mentioned in the Section 2.3 "Interaction of gamma-rays with matter". The incident photon can interact anywhere in the crystal, with a probability exponentially decreasing with the depth.

Next, the scintillation process can occur, generating several photons. Each interaction of an ionizing particle with the medium leads to the excitation of the atoms in a small volume compared to the crystal dimensions, i.e. a sphere of about 100 μm radius followed by an isotropic scintillation photons emission. The consequent transist of these photons from the interaction point to the photodetector can severely affect the detector performance, leading to delays and absorption losses.

A fraction of scintillation photons is absorbed by the crystal bulk, and the other fraction can be subject to reflection losses at the crystal interfaces. The absorbed fraction depends on crystal transparency to its own radiation, which is related to crystal's attenuation coefficient for the emission wavelength. LYSO emission wavelength is 420 nm, while GAGG emission wavelength is 520 nm. On the other hand, LYSO's attenuation coefficient at 420 nm is about 0.25 mm^{-1}, while GAGG's attenuation coefficient at 520 nm is 0.010 mm^{-1} [39].

The attenuation coefficient is, by definition, the fraction of attenuated incident photons in a monoenergetic beam per unit thickness of a material. It can be noted that attenuation coefficient of GAGG:Ce is 96 % smaller than LYSO:Ce's, for the corresponding scintillation emission wavelength. This means photons from scintillation process are more absorbed by LYSO:Ce, and GAGG:Ce is able to emit a larger number of detectable photons. In fact, for the same conditions of wrapping and readout, previous studies measured 42% larger light output for GAGG:Ce over LYSO:Ce, and transparency can be one of the contributions.

On the other hand, among the photons that are not absorbed, only a fraction of them reach the detector area. This fraction depends on the angle at which they are emitted, on the refractive index of the crystal used and on the refractive index of optical matching media. The rest of the photons escape from the crystal or remain trapped inside the crystal.

Light path without any wrapping

Let's first consider a LYSO:Ce crystal without any wrapping, and silicon grease (with refractive index of 1.55) as optical matching media between crystal and photodiode. Different propagation modes can be identified, as represented in Figures 4.4 to **??** and Table 4.1. As the emission is isotropic and the the crystals are symmetric in x, y and z directions, the calculations are made for half sphere.

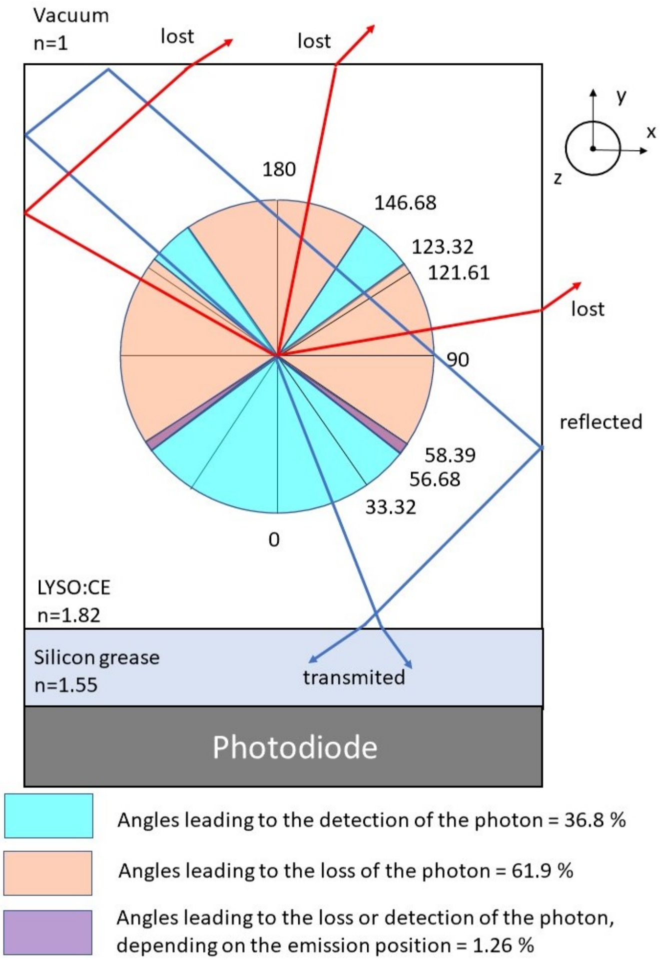

Figure 4.4: Propagation modes inside LYSO:Ce crystal with no wrapping and silicon grease as optical matching between crystal and photodiode.

Emission Angles (º)	**Description**	%
$0< \theta <90-\sin^{-1}(1/1.82)$	Photons directly hit the silicon grease region or hit the side wall first being totally reflected, and hit the silicon grease afterwards. Can be detected.	22.5
$90-\sin^{-1}(1/1.82)< \theta < \sin^{-1}(1.55/1.82)$	Depending on the interaction position, photons can reach directly the silicon grease or hit the side wall and escape the crystal. In the last case, the angle is not big enough to induce total reflection.	1.3
$\sin^{-1}(1.55/1.82)< \theta <90+\sin^{-1}(1/1.82)$	Photons are lost to air as the angles are smaller than critical angle for LYSO-vacuum interface.	53.7
$90+\sin^{-1}(1/1.82)< \theta <180-\sin^{-1}(1/1.82)$	Photons are emitted to the opposite direction of silicon grease region, however the angle is larger than LYSO-vacuum critical angle and photons are totally reflected three times, and end up reaching silicon grease region.	14.3
$180-\sin^{-1}(1/1.82)< \theta <180$	Photon are emitted backwards and hit the crystal side in a angle smaller than critical angle for LYSO-vacuum interface, such that they escape the crystal.	8.2

Table 4.1: LYSO:Ce crystal with silicon grease scintillation photons propagation modes

According to Table 4.1, for LYSO:Ce crystal with silicon grease as optical matching media, a total of 36.8 % of photons reach the silicon grease region directly. 63.2 % of the emitted photons are lost to vacuum, considering the interaction position-dependent small portion is lost.

The equivalent schemes of Figure 4.4 for GAGG:Ce are in Figure 4.5. Following the same procedures, the loss percentages for GAGG:Ce were obtained, using first silicon grease as the optical medium, and then NOA 169 glue (with refractive index of 1.69). The results are presented in Table 4.2.

Crystal	**Optical medium**	**Losses (%)**
LYSO:Ce (n=1.82)	Silicon grease (n=1.55)	63.2
GAGG:Ce (n=1.90)	Silicon grease (n=1.55)	60.1
GAGG:Ce (n=1.90)	NOA 169 glue (n=1.69)	56.7

Table 4.2: Predicted losses of emitted scintillation photons for LYSO:Ce and GAGG:Ce, silicon grease and NOA 169 glue.

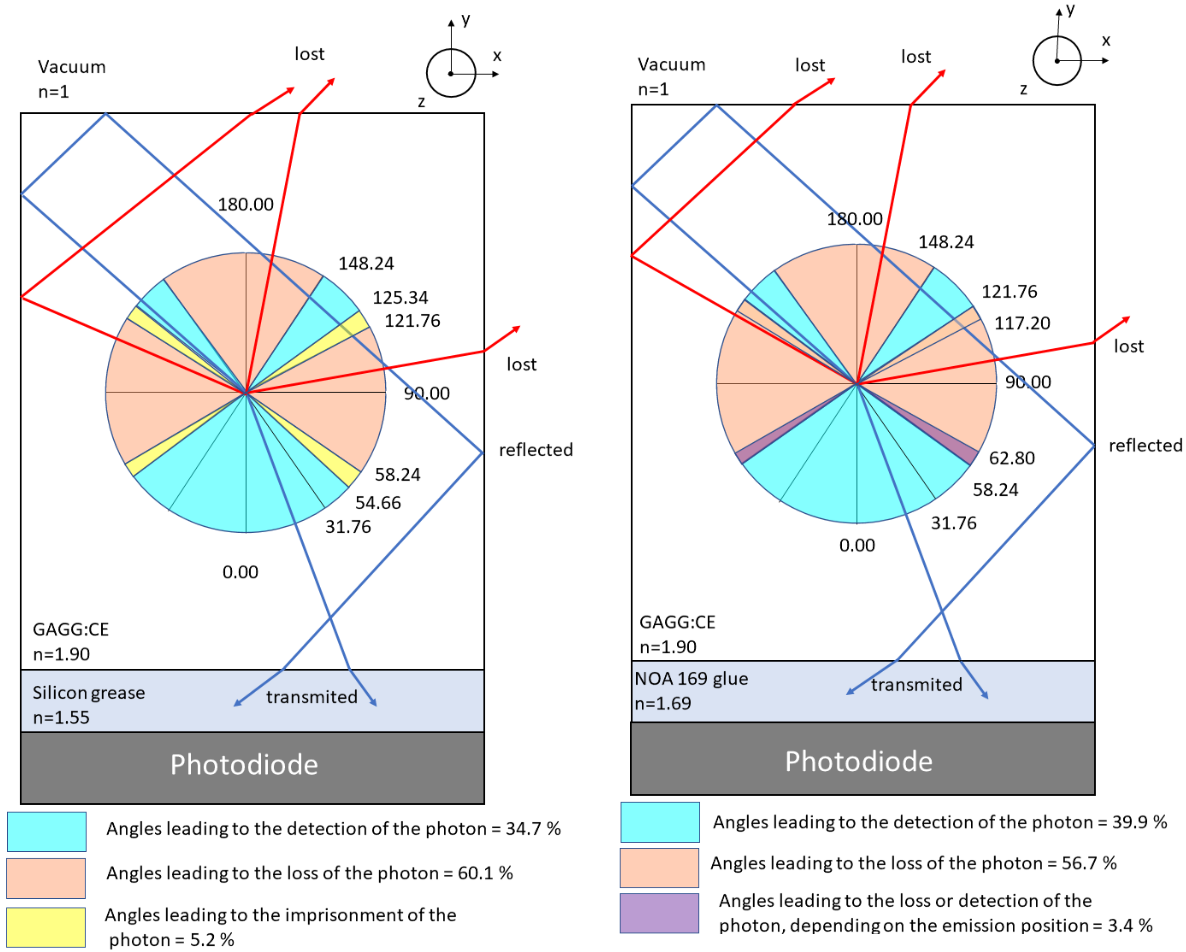

(a) Light path scheme inside GAGG:Ce with silicon grease

(b) Light path scheme inside GAGG:Ce with NOA 169 glue

Figure 4.5: Propagation modes inside GAGG:Ce crystal.

This simple analysis indicates, one more time, that GAGG is capable of a higher light output compared to LYSO, in terms of optical path of photons. In addition, we note that NOA 169 glue increases the light collection compared to silicon grease due to its bigger refractive index.

Fresnel losses

Until now, for angles up to critical angles, transmittances in crystals-surrounding interfaces have been considered to be 100%. In fact, a fraction of lost photons are in fact reflected back. The larger the reflectance at crystal-vacuum interface, more photons can be recovered. On the contrary, at crystals-optical medium interfaces, the greater the transmittance, the more photons can be detected. In the Table 4.3 are presented the calculated reflectances or transmittances for each crystal-surrounding interface, based on Equations 2.19 to 2.22. These values were calculated for all the angles lower than the critical angle.

GAGG allows a little more reflectance in crystal-vacuum interface, but LYSO allows a slight increase in crystal-optical medium transmittance. NOA 169 glue leads to a larger trasmittance compared to silicon grease.

Parameters	**LYSO-vacuum reflectance**	**GAGG-vacuum reflectance**	**LYSO-Si grease transmittance**	**GAGG-Si grease transmittance**	**GAGG-NOA 169 transmittance**
Values	18.80 %	21.01 %	95.21 %	93.97 %	95.97 %

Table 4.3: Parameters for prediction of gamma-ray losses in crystal entrances

Light path with wrapping

When wrapping is added to the external crystal faces, part of lost photons can be redirectioned into the crystal again, being recovered for detection. Let's suppose the surfaces are polished and wrapping is perfectly attached to three crystals faces (to leave free the gamma-rays input face and the opposite one). Teflon is a diffusive wrapping while aluminized mylar and aluminized kapton allow mostly specular reflections. It's expected that any of these wrappings increase light output, however specular reflectors may lead to more multiple reflections, or even trapped photons, inside the crystal.

Conclusion

Summarizing, we expect a higher emission transparency of GAGG:Ce over LYSO:Ce, associated with a higher photosensitivity from unsealed photodiode to GAGG:Ce scintillation. In addition, are expected lower scintillation photons losses to vacuum when using GAGG:Ce, specially when teflon wrapping is aplied. Furthermore, we predict lower Fresnel losses for GAGG:Ce with NOA 169 glue and unsealed photodiode. This lead us to expect a better light collection for GAGG:Ce crystal, teflon, NOA 169 and unsealed photodiode combination.

Chapter 5

Methods

In order to obtain the scintillator with the best light output and energy resolution, several combinations of crystal, wrapping, optical matching media and silicon PIN photodiode were evaluated by comparing the ^{137}Cs spectra emitted by one cesium radioactive source and measured with each evaluated detector. In the present section, the main materials used in this study are presented, followed by the description of the procedures followed, since the detectors mounting, spectrum acquisition chain and data analysis.

5.1 Evaluated components

As seen in Figure 5.1, the evaluated crystals are GAGG:Ce and LYSO:Ce. For wrapping we tested aluminized kapton, aluminized mylar and teflon. Silicon grease and NOA 169 glue were the optical matching media analysed and finally, sealed and unsealed photodiodes were evaluated.

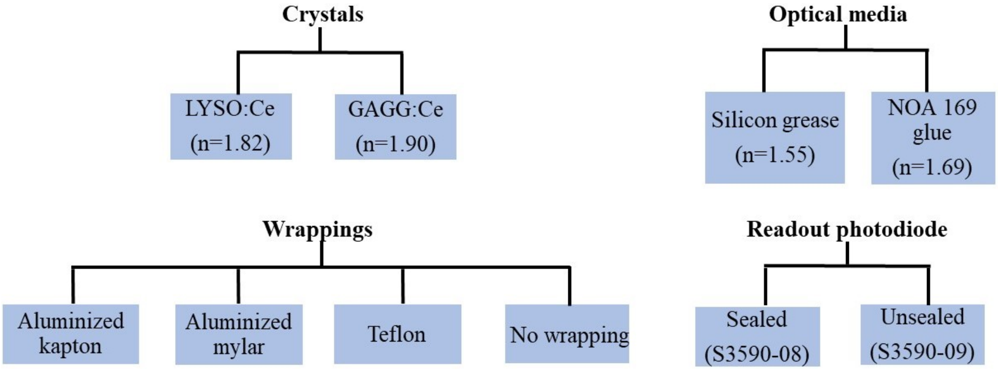

Figure 5.1: Options for crystal, wrapping, readout and optical media

LYSO:Ce and GAGG:Ce are fast, high density, high light output and high refractive index scintillator crystals. This crystals allow small and efficient solutions to detect high energy radiation. While GAGG:Ce has a larger light output, LYSO:Ce presents a faster decay time. In addition, another difference between the two crystals is that LYSO present intrinsic radioactivity and GAGG does not. The radioactive element in LYSO is ^{176}Lu which decays via β^- with a continuum spectrum of energies from zero to E_{max}=593 keV, to ^{176}Hf. This is followed by the emission of gamma rays (γ_1, γ_2 and γ_3 with energies of 307, 202 and 88 keV, respectively). Related internal conversion processes compete with the emission of γ_2 and γ_3, as a result of the isomeric transitions of the excited states of ^{176}Hf. Figure 5.2 presents a scheme of ^{176}Lu decay and an example of the correspondent spectrum for a large (57.4 × 57.4 × 10 mm^3) crystal used at Enríquez-Mier-y Terán et al. [38].

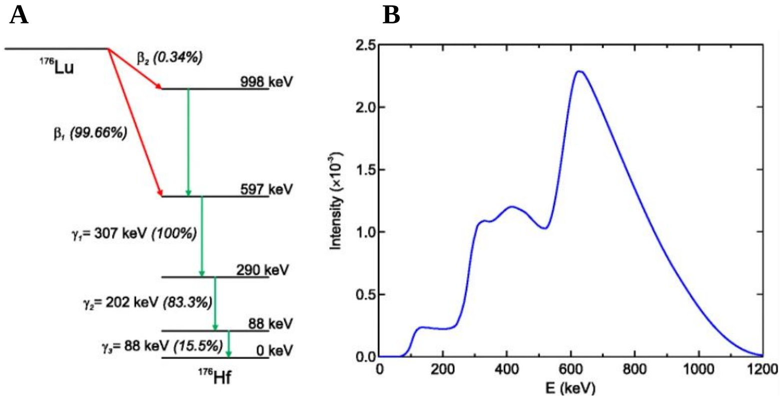

Figure 5.2: (A) Decay scheme of ^{176}Lu, and (B) experimental measurement of energy spectrum due the intrinsic radiation of a LYSO crystal (57.4 × 57.4 × 10 mm^3). Image from [38].

The intrinsic radioactivity accounts for approximately 300 Bq/cm^3, which produces a rate of events that usually cannot be ignored. This emission is isotropic with a half-life of 3.76×10^{10} years [38].

The crystals used in this work were manufactured and commercialized by Epic-crystal. The main crystals's features are indicated in the Table 3.1. The dimensions of the used GAGG:Ce and LYSO:Ce are 1 cm x 1 cm x 1 cm.

Regarding the wrapping materials, aluminized kapton came around LYSO:Ce crystal from the manufacturer and as such, no detailed information was presented related to it. Aluminized mylar is a thin film which is aluminum in one side and mylar on the other side. Teflon is a white film, thicker than aluminized mylar. Teflon and aluminum are the most common wrapping materials as they are efficient, cheap and easy to use.

The used optical matching media were the general purpose silicon grease with refractive index of 1.55 and a high refractive index glue (1.69). This media were used not only to improve optical transfer between different index materials, but also to attach them together. The high refractive index glue has product name: Norland Optical Adhesive NOA 169 by Norland Products, Inc (NOA 169) commercialized by AMS Technologies and presents the following characteristics:

Name	**NOA 169**
Temperature range	-15° C to 100° C
Glass bonding	Excellent
Plastic bonding	Excellent
Metal bonding	Good
Durability	Hard and brittle
Viscosity (cps)	4500 - 5500
Shelf life	4 months
Energy for full cure (J/cm^2)	6
Absorption range (nm)	315 - 450

Table 5.1: NOA 169 glue features

NOA 169 glue has an effective UV curing, as the peak absorption is 365 nm. However, it can also be cured with visible light from 400 nm to 450 nm. It requires 6 J/cm^2 to fully cure, which in practice implies around 10 minutes in the UV lamp present in our laboratory, or several hours at visible light. This NOA 169 glue is no longer manufactured.

Finally, the evaluated readout photodetector consists of a silicon PIN type photodiode from S3590 series from Hamamatsu. The sealed photodiode is from S3590-08 type and is covered by one epoxy resin window, while unsealed photodiode is from S3590-09 type having no window. Their main features are indicated in the Table 5.2.

Si PIN photodiode	**S3590-08**	**S3590-09**
Window	Sealed (epoxy resin)	Unsealed
Photosensitive area (cm)	1 x 1 x 1	
Reverse voltage max Vr (V)	100	
Power dissipation (mW)	100	
Operating temperature (ºC)	- 20 to + 60	
Spectral response range (nm)	340 - 1100	
Peak sensitivity wavelength (nm)	960	
Dark current Vr=70 V (nA)	2	
Cutoff frequency Vr=70 V (MHz)	40	

Table 5.2: Si PIN photodiodes features

It can be noticed from Tables 3.1 and 5.2 that the emission wavelength of both LYSO:Ce and GAGG:Ce (420 and 520 nm) are within sensitive range of photodiodes (340 to 1100 nm) which is a crucial factor to ensure detection of scintillation photons. The photosensitivity for the spectral response range of these S3590 photodiodes is presented in the Figure 4.3. In addition, this photodiodes operate in a temperature range that includes our initial requirement of -10ºC to +50 ºC. Also they are small, low noise, low power consumption and common use devices.

5.2 Detectors mounting and setup

The general detector setup used for experimental measurements in this work is the setup considered in the Chapter 4 "Theoretical assessment", presented in the Figure 4.1. The analysed combinations of detector components are identified in Figures 5.3 and 5.4 as well as the corresponding numbering for further identification. For example, experiment nº 2 uses GAGG:Ce, without wrapping, silicon grease and sealed Si PIN photodiode.

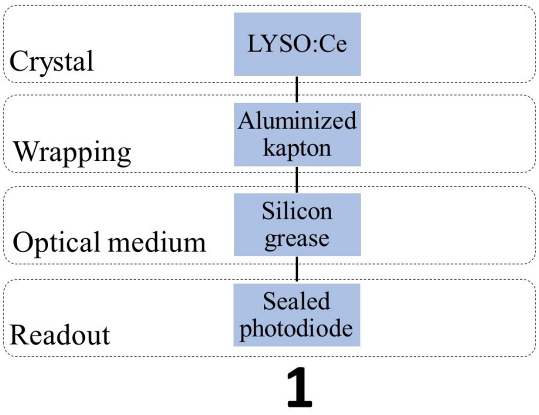

Figure 5.3: Evaluated combination of scintillator detector components using LYSO:Ce

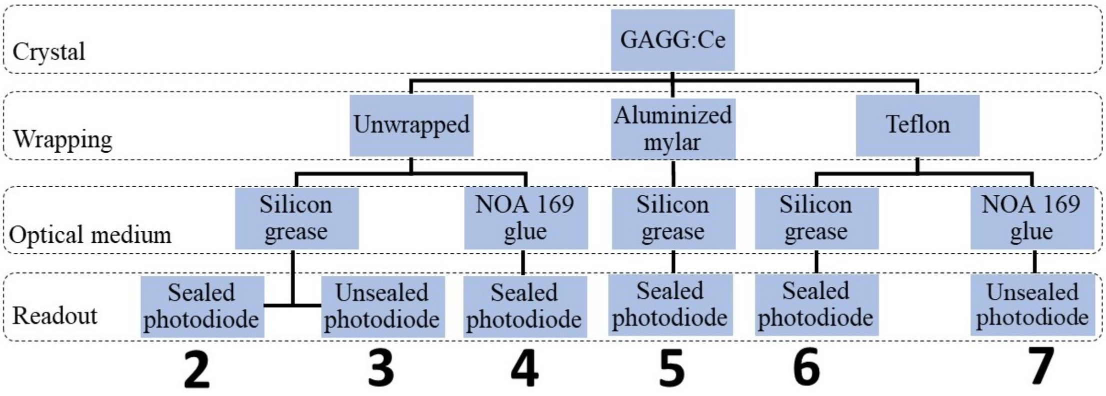

Figure 5.4: Evaluated combination of scintillator detector components using GAGG:Ce

All the operations of wrapping and gluing the crystals onto the photodiode were done in a clean room located in the ICT City, University of Turku, Finland. The operators wore a protective suit that covered the entire body and clothing except the face. Inside the clean room, it was also mandatory to wear a mask, hair cap and gloves in order not to contaminate the materials. The materials that went into the clean room from the outside entered through a side door and were cleaned with ethanol to remove grease and contaminants.

To apply silicon grease and NOA 169 between photodiodes and crystals, a small drop of glue was added in the middle of the photodiode. Next, the crystal was placed on top, vertically, in order to spread the glue drop evenly in all directions. The glue application was inspected in a microscope afterwards, to guarantee that no air bubbles were kept in the interface. To fix the wrapping to the crystals, NOA 169 glue was used. The glue application was performed applying a thin layer of glue over all the crystal faces to be covered. Afterwards, a cut band of wrapping material was carefully applied around the target crystal faces, being pressed slowly always in the same direction.

After the applications, the assemblies were taken to cure the glue. NOA 169 curing was made by means of 15 minutes under UV lamp in the clean room. In most cases, the expected 15 minutes in UV lamp was not enough, probably due to blocking of UV by crystal itself and wrappings. In this cases, the assembly was taken to oven at 150 $^{\text{o}}$C for 30 minutes. After it, the materials were left to cool down at room temperature. Next, a inspection of glue hardness was carried out, and in case of success in glue curing, the assembly was ready to perform measurements.

The crystals faces covered by wrapping vary from case to case. In experiments 1 and 5, the wrapping covers 4 lateral faces of crystal as represented in Figure 5.5, being one of the lateral faces the input face for radiation from ^{137}Cs source. However, while in experiment 1 the wrapping was made by the manufacturer, in experiment 5, aluminized mylar wrapping was made by hand. Figures 5.6a and 5.6b are real pictures of experiment 1 and 5, soldered to a green PCB which simply connects the signal to the electronic signal conditioning system, presented in the Section 5.4 ”Spectrum acquisition chain”.

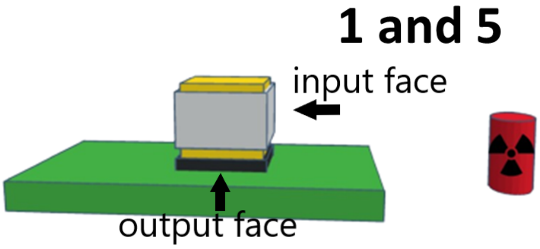

Figure 5.5: Schematic setup of experiment 1 and 5. Red: radioactive ^{137}Cs source. Yellow: scintillator crystal. White: wrapping material. Black: photodiode. Green: PCB to connect detector to electronic signal conditioning system.

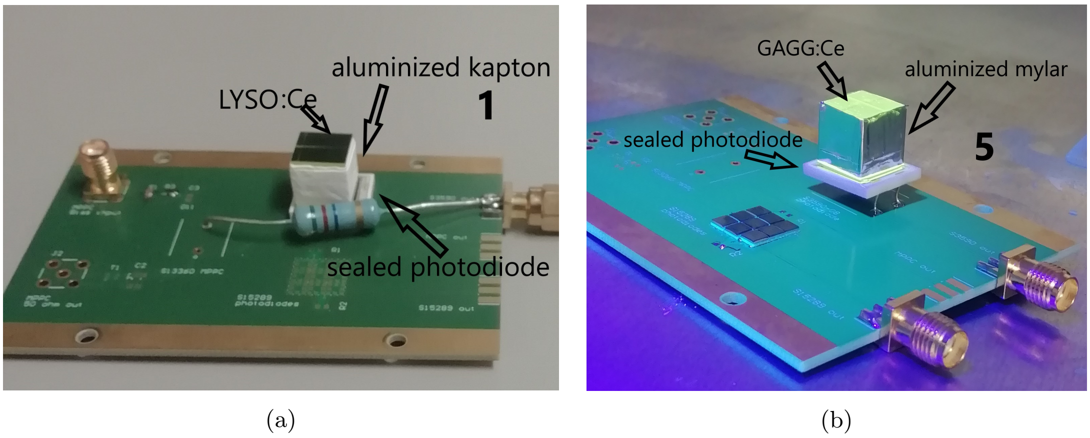

(a)

(b)

Figure 5.6: Pictures of experiment 1 (a) and experiment 5 (b).

In experiment 6, all the faces except the output one are covered, and the wrapping was applied by hand (see Figure 5.7). Finally, in experiment nº 7, only 3 faces are covered, the top face and two opposite lateral faces, also by hand. In such a way that, the gamma rays coming directly from radioactive source hit a free crystal face (see Figure 5.8).

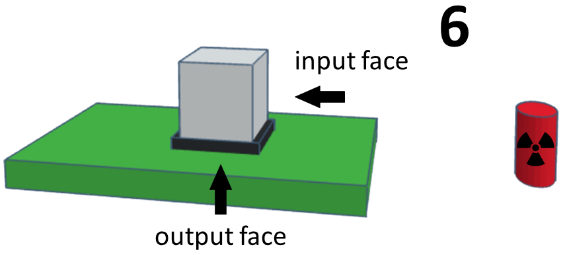

Figure 5.7: Schematic setup of experiment 6. Red: radioactive ^{137}Cs source. White: teflon. Black: sealed photodiode. Green: PCB to connect detector to electronic signal conditioning system.

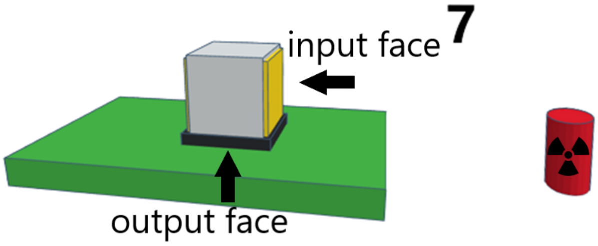

Figure 5.8: Schematic setup of experiment 7. Red: radioactive ^{137}Cs source. Yellow: GAGG:Ce crystal. White: teflon. Black: unsealed photodiode. Green: PCB to connect detector to electronic signal conditioning system.

5.3 ^{137}Cs Spectrum

In order to evaluate the performance of each tested detector, a radioactive source of cesium 137 (^{137}Cs) was used to provide incident radiation. The ^{137}Cs decay scheme is presented in Figure 5.9.

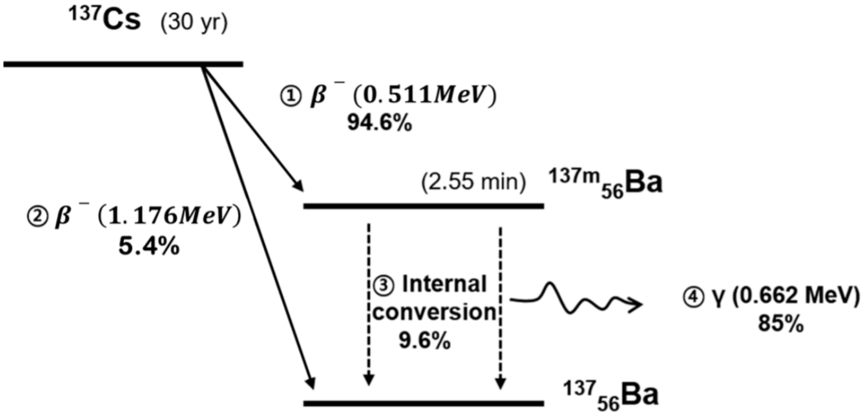

Figure 5.9: ^{137}Cs decay scheme. Image from [26].

The radioactive isotope cesium-137 (^{137}Cs) has a half-life of about 30.17 years. About 95% of the decays correspond to beta emission to a metastable nuclear isomer of barium: ^{137m}Ba. The remainder decays from ^{137}Cs directly populate the ground state of ^{137}Ba, which is stable. ^{137m}Ba decays also to the ground state, with a half-life of about 153 seconds emitting gamma rays with 0.6617 MeV energy. A total of 85.1% of ^{137}Cs decay generates gamma ray emission in this manner. 32 keV peak is also emitted by ^{137m}Ba during internal conversion from excited states [26].

The general emission spectrum of ^{137}Cs is presented in Figure 5.10.

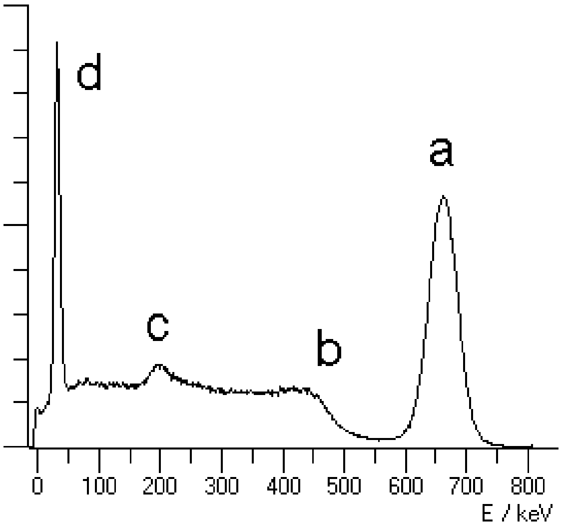

Figure 5.10: General ^{137}Cs spectrum outline. (a) is the 661.7 keV photopeak, (b) is the Compton edge, (c) is the backscattering photopeak and (d) is the 32 keV internal conversion photopeak

The monoenergetic γ photon of energy E_γ=661.7 keV can be completely absorbed originating photopeak (a). On the other hand, the γ photon can suffer Compton collisions outside the detector which leads to an energy loss of the photon before it reaches the detector. A continuum of scattered photons arises with energies from E_γ (661.7 keV) down to the energy after 180° backscattering (point (c) in the spectrum). The photopeak (c) arises from the angular dependence of the scattered energy with the scattering angle, in which nearly identical energies result from angles greater than about 110-120º.

On the other side, it can also occur that the γ photon suffers Compton scattering inside the crystal and escapes from the detector, being only detected the energy of the electron. The energy of this electron lies between zero and the maximum value, which corresponds to 180° backscattering, leading to a continuum from zero up to the Compton edge (478 keV, peak (b)) [17].

5.4 Spectrum acquisition chain

To obtain the ^{137}Cs spectra, an acquisition chain was followed which is presented in Figure 5.11. Generally, it starts with the scintillator crystal which emits photons whose intensity is proportional to the energy deposited in the crystal by the incident particle, and therefore proportional to the energy of incident radiation. Next, the photodiode collects these scintillation photons converting it in a current pulse signal which intensity is proportional with scintillation magnitude. Thereafter, a signal conditioning system prepares the signal in order to be converted to digital next. This signal conditioning system is constituted by a Charge Sensitive Preamplifier (CSP) device and a shaping amplifier. CSP preamplifies the current signal from the photodiode, producing an output voltage signal proportional to the amount of input charge. The voltage signal is then amplified and filtered in a shaping amplifier device. Afterwards, the voltage signal is processed, being digitized in a multichannel analyser (MCA) called Digital Pulse Height Analyser by CAEN. In this, the input voltage pulses are counted based on their amplitude producing an histogram of energy against pulse amplitude. Finally, it can be sent to a computer and be displayed on a screen.

The radioactive source and the scintillator detector are positioned inside a vacuum chamber

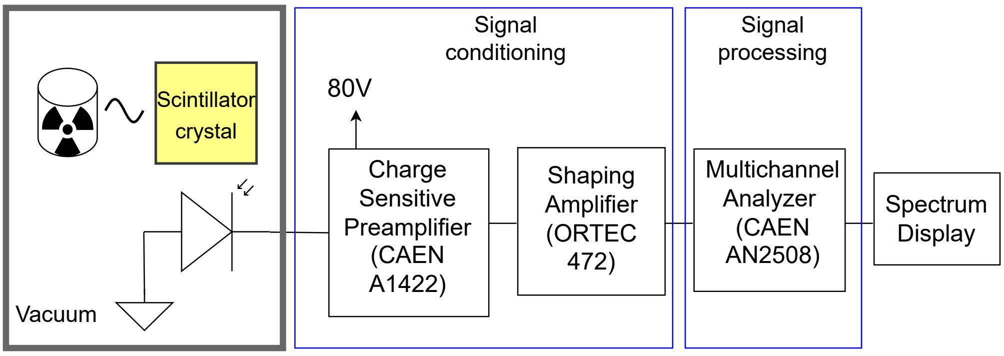

Figure 5.11: Spectrum acquisition chain scheme

with a pressure of 10^{-3} mbar or lower, with the setups presented in the Section 5.2 "Detectors mounting and setup". The photodiode is biased with 80 V through the CSP device connection, as suggested by Figure 5.11. The signal from the photodiode is an inverted pulse type current signal, as shown on Figure 5.12, top.

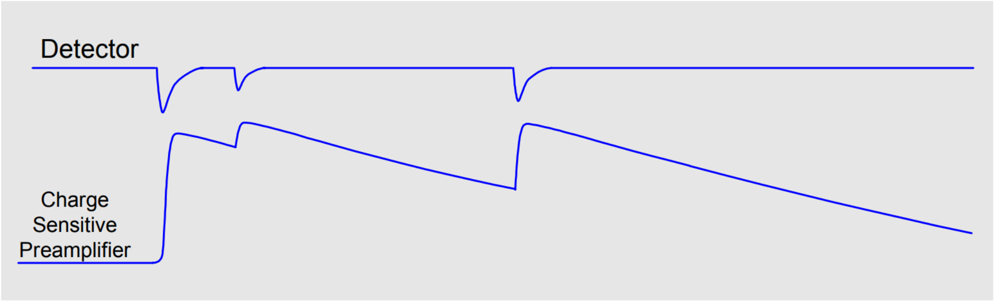

Figure 5.12: Photodiode signal output (top) and CSP signal output (bottom)

The charge sensitive preamplifier receives this signal as input and as output presents a positive tail voltage signal as shown in Figure 5.12, bottom.

The CSP used in this experiment is from A1422 series by CAEN, guaranteeing low noise, fast response and high counting rates. The given nominal sensitivity is 90 mV/MeV using a solid state silicon detector as input stage, and the nominal decay time is 50 μs. The maximum noise is 4.2 keV FWHM, also using a silicon photodetector. In the input, a voltage of 80 V is applied to bias the photodiodes, given by a four channel programmable CAEN power supply (high voltage source) from N1419 series. It is constituted by an inverting transimpedance amplifier followed by an output voltage amplifier as presented in Figure 5.13.

Next the CSP's output signal is amplified and shaped by an analog shaping amplifier from 472 series by ORTEC with adjustable gain and shaping time. This device produces an output pulse shaped like a Gaussian function, whose height is proportional to the energy deposited by incident particle in the scintillator. The use of shaping amplifiers changes the fall time of the pulse signals to a fixed value, reducing the incidence of pulse 'pile up'. It also removes high frequency noise from the input signal. The shaping time in our experiments was defined as 2 μs. On the other hand, the coarse gain was set to 200x.

Another key device in spectrum acquisition chain is the N6781 Multichannel analyzer by CAEN. This device samples the pulses output by the previous shaping amplifier device (in our case), converts them into a continuous data stream and produces an energy histogram (spectrum).

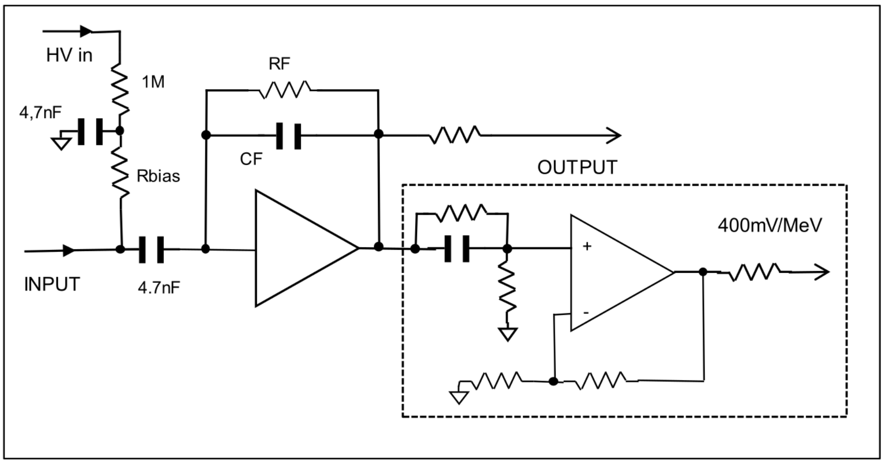

Figure 5.13: CSP general diagram

This spectrum consists on a presentation of the number of peaks detected for each channel, which corresponds to a peak amplitude and consequently to an energy of incident particle.

N6781 MCA is equipped with a FPGA providing energy (i.e. pulse height) and timing information. The analyzer is loaded with Digital Pulse Processing for Pulse Height Analysis (DPP−PHA) firmware and managed by the DPP−PHA Control Software. N6781 MCA includes a Flash Analog to Digital Converter (ADC) of the 724 series (100 MS/s, 14 bit), which digitizes continuously the analogue inputs, making the samples available to the DPP−PHA algorithm running on the FPGA. After the digitization, in order to achieve higher precision on peak height calculation, the MCA performs one more signal shaping amplification. This pulse shaping is done by means of a trapezoidal filter as shown in Figure 5.14.

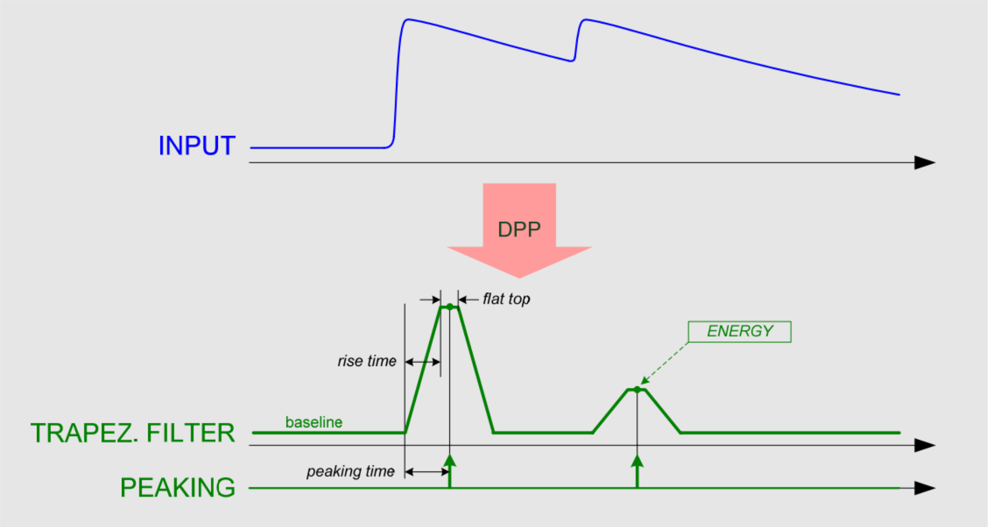

Figure 5.14: Input from CSP and MCA trapezoidal filter with the relevant parameters.

The DPP - PHA Control Software allows us to set the parameters for the acquisition, configure the hardware and perform the data readout, the histogram collection and saving. In our experiments, the acquisition parameters were kept constant from spectrum to spectrum and included input counting rate and trapezoid rise time (see Figure 5.14). The latter parameter plays the same role as the shaping time of a analog Shaping Amplifier.

The ADC converts the analog signal to digital and is a crucial component for MCA operation. In this N6781 Multichannel analyzer, the ADC is a flash ADC type. A flash ADC uses a linear voltage ladder with a comparator on each ”rung” of the ladder to compare the input voltage with successive reference voltages. Usually these reference ladders are built with several resistors. The output of these comparators is usually fed into a digital encoder, which converts the inputs into a binary value. A flash converter requires 2^n-1 comparators for an n-bit conversion.

In the Figure 5.15 below is presented a real picture of the MCA, shaping amplifier and high voltage source devices used to acquire spectra in this study.

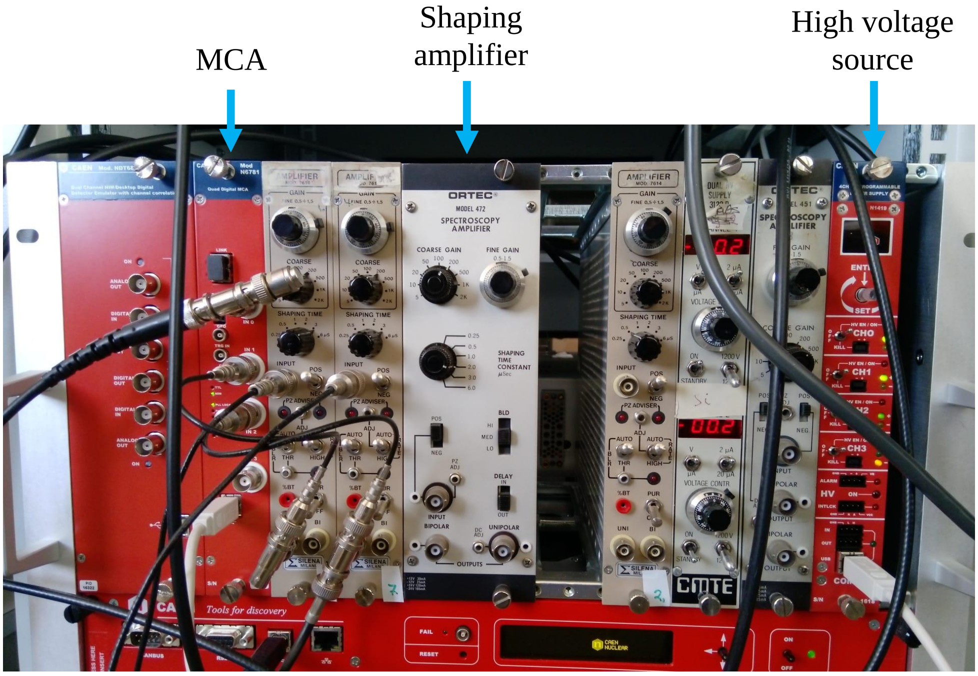

Figure 5.15: Picture of multichannel analyzer (MCA), shaping amplifier and high voltage source

To set the acquisition parameters and to display spectra histograms, the user interface consisted of a software called CoMPASS (CAEN Multi-PArameter Spectroscopy Software). For this, the MCA is connected to a computer by USB connection. Finally,the acquired spectrum is saved as a folder containing a .txt file with the spectrum counts (number of peaks detected) for each channel (related to energy values). In addition other files containing information about the acquisition are saved as well. The .txt file was next analyzed by us in order to collect information on light collection efficiency and energy resolution of the different evaluated detectors. This analysis is discussed in the next section.

5.5 Data Analysis

After the ^{137}Cs spectra are acquired, this data has to be analysed by software, using a Python script, in order to obtain information related to light collection and energy resolution of each tested detector. The relative light collection is given by the position (μ) of 661.7 keV photopeak, and the energy resolution is obtained through 661.7 keV photopeak FWHM as follows:

$$Energy\ resol. = \frac{FWMH}{\mu} \tag{5.1}$$

To obtain μ and FWHM of 661.7 keV peak of all spectra, the first step was to standardize the spectra. For this, we started by removing the low frequency noise from each spectra, deleting the peak with lower energy which corresponds to electronic noise. The noise peak counts varied from spectrum to spectrum, depending on the acquisition parameters for each case. Removing the low energy noise allowed for the elimination of data of no interest to the case and enabled clearer visualization of the data part containing information of interest. Next, a scale adjusting was applied so that all spectra were on the same scale, to facilitate comparison of the position of the peaks.

The method used to obtain FWHM and μ was based on adjusting a normal gaussian distribution on 661.7 keV photopeaks data. To this gaussian photopeak originated by the gamma photons from the source, a background radiation is added and must be removed before the adjusting, as suggested in Figure 5.16. This background contribution has a linear behaviour, decreasing with the energy. Therefore, the background was subtracted from the peaks.

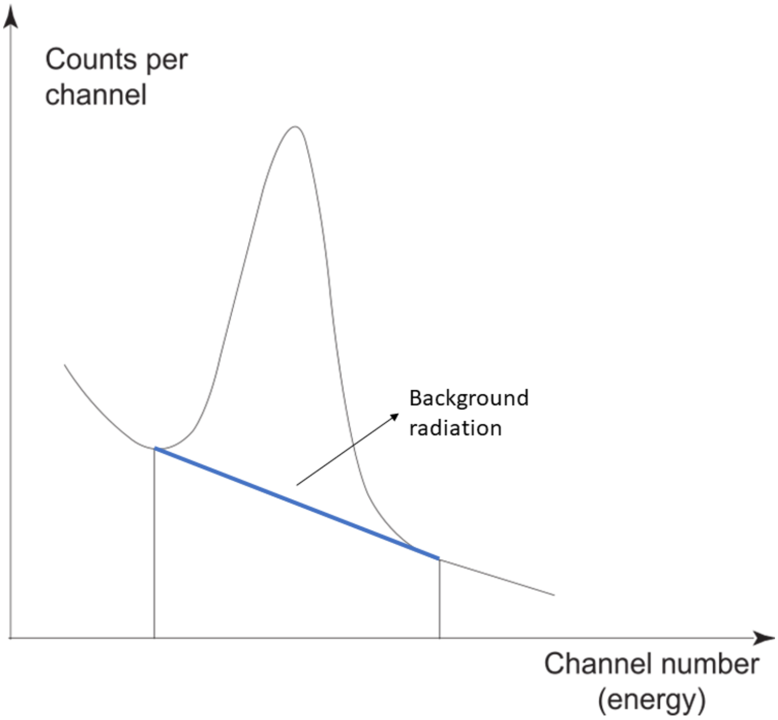

Figure 5.16: Spectrum photopeak added to background radiation

After the linear base trend subtracting, the gaussian function was fitted to the photopeak experimental data and it's mean (μ) and standard deviation (σ) were acquired. The gaussian function ($f(x)$) is generally given by:

$$f(x) = \frac{1}{\sigma\sqrt{2 * \pi}} e^{-(x-\mu)^2/(2\sigma^2)} \tag{5.2}$$

The photopeak position is given directly by the mean μ of the obtained gaussian function, while FWHM is obtained by gaussian distribution on 661.7 keV photopeaks data and acquire it's mean and standard deviation (σ) [25] as follows:

$$FWHM = 2\sigma\sqrt{2ln2} = 2.35\sigma \tag{5.3}$$

This analysis was made implementing a python script. This script had as input the spectra .txt file containing raw data from CoMPASS software and has output had figures which include the standardized acquired spectra and 661.7 keV photopeak gaussian adjust with the corresponding FWHM, position (μ), and energy resolution. The linear base trend was obtained adjusting one linear function to the two extreme points of the photopeak of interest using polyfit function of Python numpy library. On the other hand, the gaussian function fitting the experimental data of the peak, as well as values uncertainties were obtained using "curve_fit" function of "optimize" package from "scipy" library.

Chapter 6

Results and discussion

For each evaluated detector, the ^{137}Cs energy spectrum was acquired in vacuum, with the general setup presented in the Section 5.2 ”Detectors mounting and setup”. The position and FWHM 661.7 keV photopeak of ^{137}Cs energy spectrum are the measures of light output and resolution. A larger photopeak means higher light output, while a lower FWHM indicates a better energy resolution.

6.1 Results

The acquired spectra for each situation are presented in Figures 6.1 to 6.7. In addition, the gaussian adjust of 661.7 keV photopeak for each spectra are presented in Figures 6.8 to 6.14. In these figures, two input parameters related to spectrum acquisition are indicated: Coarse gain and Real Time, both associated to MCA operation and selected through CoMPASS software. Coarse gain is the gain applied in the channel axis, and Real Time is the time during which counts had been acquired for spectra generation in the format hours:minutes:seconds. In addition, the three important parameters characterizing the experimental 661.7 keV photopeaks are also presented: mean (μ), which represents its position, FWHM and energy resolution, obtained from gaussian adjust.

The main results are summarized in the Table 6.1.

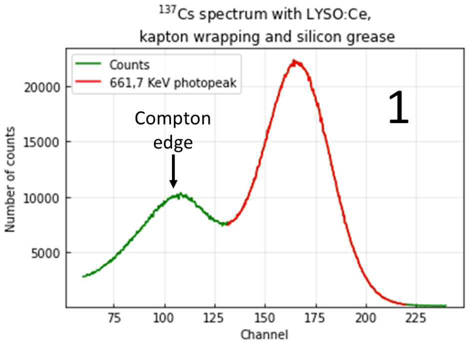

Figure 6.1: Obtained spectrum of experiment 1

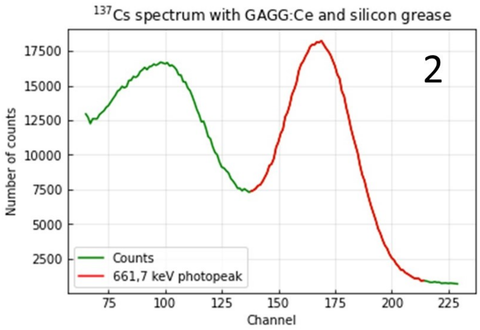

Figure 6.2: Obtained spectrum of experiment 2

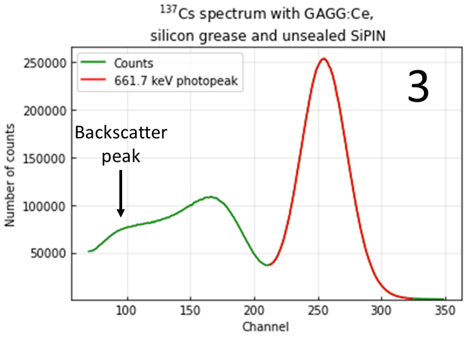

Figure 6.3: Obtained spectrum of experiment 3

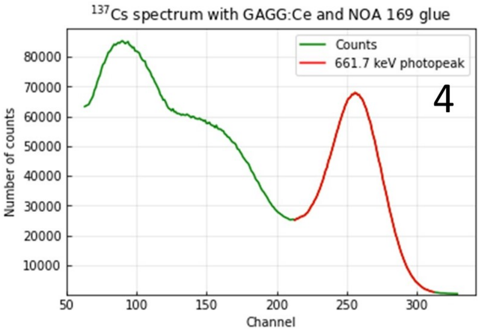

Figure 6.4: Obtained spectrum of experiment 4

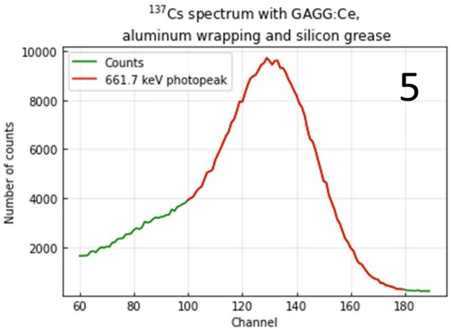

Figure 6.5: Obtained spectrum of experiment 5

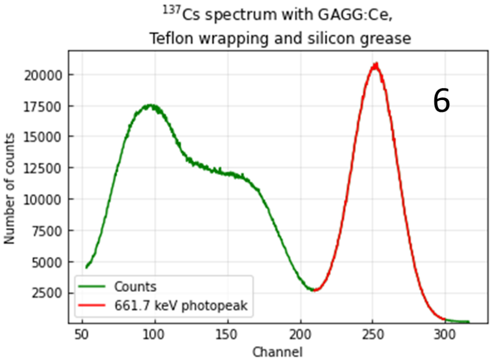

Figure 6.6: Obtained spectrum of experiment 6

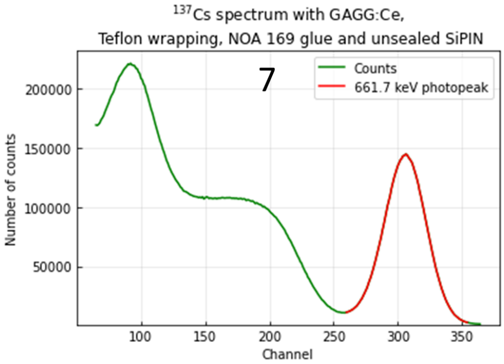

Figure 6.7: Obtained spectrum of experiment 7

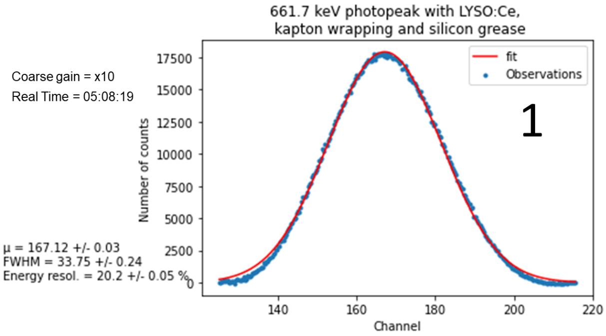

Figure 6.8: Gaussian adjust of 661.7 keV photopeak from experiment 1

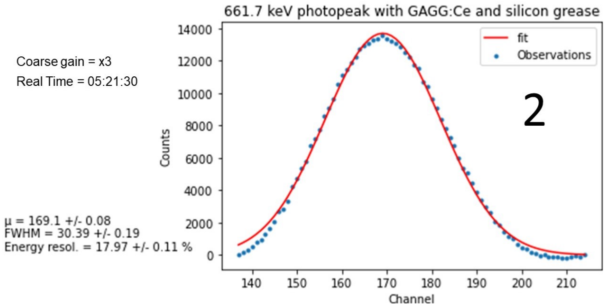

Figure 6.9: Gaussian adjust of 661.7 keV photopeak from experiment 2

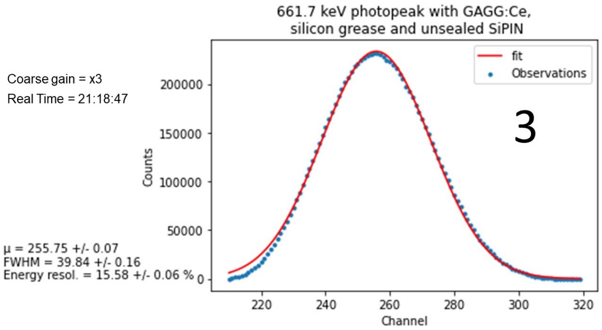

Figure 6.10: Gaussian adjust of 661.7 keV photopeak from experiment 3

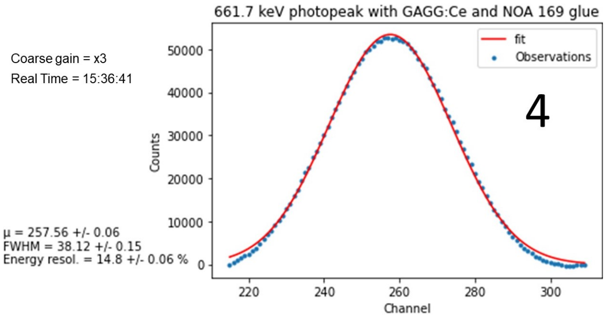

Figure 6.11: Gaussian adjust of 661.7 keV photopeak from experiment 4

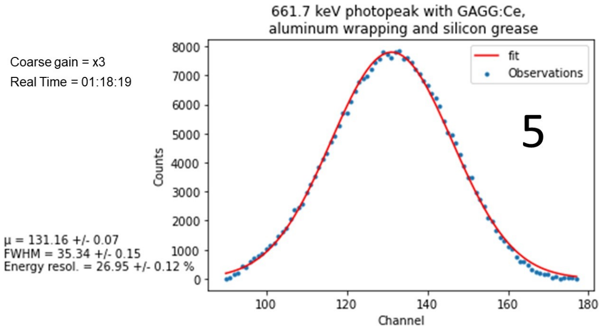

Figure 6.12: Gaussian adjust of 661.7 keV photopeak from experiment 5

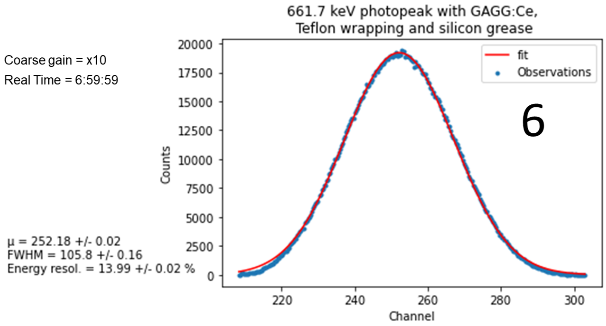

Figure 6.13: Gaussian adjust of 661.7 keV photopeak from experiment 6

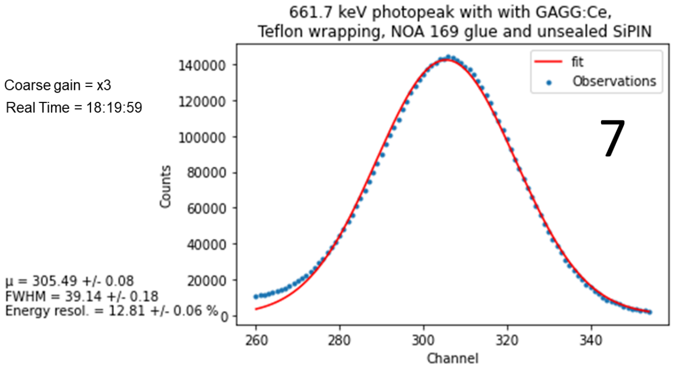

Figure 6.14: Gaussian adjust of 661.7 keV photopeak from experiment 7

Detector	**Crystal**	**Photodiode**	**Glue**	**Wrapping**	**661.7 keV peak μ**	**661.7 keV peak energy resol.**
1	LYSO:Ce	Sealed	Silicon grease	Alumin. kapton	167.12 ± 0.03	20.2 ± 0.05 %
2	GAGG:Ce	Sealed	Silicon grease	-	169.1 ± 0.08	17.97 ± 0.11 %
3	GAGG:Ce	Unsealed	Silicon grease	-	255.75 ± 0.07	15.58 ± 0.06 %
4	GAGG:Ce	Sealed	NOA 169	-	257.56 ± 0.06	14.80 ± 0.06 %
5	GAGG:Ce	Sealed	Silicon grease	Alumin. mylar	131.16 ± 0.07	26.95 ± 0.12 %
6	GAGG:Ce	Sealed	Silicon grease	Teflon	252.18 ± 0.02	13.99 ± 0.02 %
7	GAGG:Ce	Unsealed	NOA 169	Teflon	305.49 ± 0.08	12.81 ± 0.06 %

Table 6.1: Summary table of main results

6.2 Interpretation

Experiment 1 was the only one with LYSO:Ce crystal, together with aluminized kapton foil as wrapping, silicon grease and sealed photodiode. In the acquired spectrum, the 661.7 keV photopeak corresponding to ^{137}Cs gamma emission can be identified, as seen in Figure 6.1. Compton edge is also detectable, with intrinsic radioactivity of LYSO added. These two photopeaks are the only distinguishable key features in this ^{137}Cs spectrum, meaning the sensitivity and energy resolution of this detection system are not enough to distinguish any other spectrum key feature. Sensitivity is related, specially, to electronic noise level which includes photodiode noise and signal conditioning noise. The 661.7 keV peak position is 167.12 ± 0.03 channels while the FWHM of 661.7 keV peak is 101.25 ± 0.24 channels, corresponding to an energy resolution of 20.2 ± 0.05 %.

Experiment 2 photodiode and optical medium are the same as the previous one, but with GAGG:Ce crystal instead of LYSO:Ce and without any wrapping. This change moved the 661.7 keV photopeak to channel 169.1 ± 0.08, and changed FWHM to 30.39 ± 0.19 channels corresponding to an energy resolution of 17.97 ± 0.11 %. This indicates that, even without any wrapping, the light output increased 1.18 % and energy resolution improved from 20.2 % to 17.97 % using bare GAGG crystal instead of LYSO wrapped with an aluminized kapton foil. This agrees with what was expected, because it was predicted before that GAGG would have higher light output than LYSO, due to larger critical angle with the surroundings and less absorption of emission wavelength. Sensitivity is still not enough to detect other key features of ^{137}Cs spectrum.

By changing the sealed photodiode by the unsealed photodiode, experiment 3 arises. It's theoretical expected one improvement on light collection, as there is one less medium in the path of light to generate absorptions and reflections. In practice, removing the epoxy resin window from the Si PIN photodiode, the light collection improved 51.12 % compared with the use of a sealed Si PIN photodiode, keeping the remainder conditions. Energy resolution is 15.58 ± 0.06 % in this case. In Figure 6.3, it can be noted that, in addition to compton edge, backscatter peak can be now identified as well, meaning an improvement on sensitivity. The sensitivity is below 300 keV, which is the minimum energy to detect by REPE. This means our detector allows a noise level lower than 300 keV, even when electronic noise is added by signal conditioning electronics.

On the other hand experiment 4 is similar to experiment 2, but using NOA 169 glue instead of silicon grease, as optical matching medium between GAGG:Ce and the sealed photodiode. The result of experiment 4 is one further improvement in light collection and energy resolution regarding previous detectors. 661.7 keV peak position is 257.56 ± 0.06 channels, which corresponds to an improvement of 52.29 % in light collection using NOA 169, compared with the case of silicon epoxy use (experiment 2). In addition, FWHM is 38.12 ± 0.15, meaning energy resolution is 14.8 ± 0.06 %.

In experiments 5, 6 and 7, wrapping was added to GAGG:Ce crystal. In experiment 5, the material is aluminized mylar, and no improvement in light collection was observed, regarding any previous detector. On the other hand, in detector nº 6, using teflon, the light collection proved to be the best so far. It would be expected that both, aluminized mylar and teflon wrapping would improve light collection. The main reason why aluminized mylar hasn't allowed improvements in light output compared to experiment 2, may be that aluminum is a specular reflector may lead photons trapping inside the crystal. Furthermore, non homogeneity in optical matching media application may have worsened light collection. Lastly, the top face of crystal was not covered by wrapping in this case (see Figure 5.6b). The covering of top face could have avoided some scintillation photons losses.

In contrast, the use of teflon wrapping in all 5 faces (experiment 6), led to an improvement of 49.1 % in light output, comparing with experiment 2 that uses unwrapped GAGG, keeping the remainder conditions. Additionally, energy resolution became 22 % better than experiment 2. In addition, in experiment 6, teflon was placed in all 5 faces, which improved detector performance, when compared with experiment 5. Also, teflon is a diffusive reflector, dispersing photons in all directions inside the crystal which avoids photons trapping.

Finally, the experiment nº 7 achieved the overall best results, among all the evaluated combinations. 661.7 peak is positioned at channel 305.49 ± 0.08, corresponding to an improvement of 21.1 % in light collection comparing to experiment nº 6, meaning an improvement of 82.8 % comparing to experiment n º1. Energy resolution of 12.81 ± 0.06 % is the best value achieved. Furthermore, from Figure 6.7, we can note that backscatter peak is detectable with experiment nº 7 setup, and is located below channel nº 100. Therefore, sensitivity of this system is, at least, 220 keV deposited in crystal scintillator. This value is below 300 keV limit for REPE.

In summary, the optimized detector consists of GAGG:Ce crystal with teflon wrapping, unsealed SiPIN photodiode (S3590-09 from Hamamatsu) and NOA 169 glue as optical matching medium between crystal and photodiode. This combination of elements provided the best light output and energy resolution. This is in line with what was expected in the Chapter 4 ”Theoretical assessment”, where the same combination of components was indicated as the one that would lead to better results. The key reasons of the performance of this detector are the high light yield of GAGG:Ce, its high transparency, non intrinsic radioactivity, optimized Teflon wrapping setup (Figure 5.8) and good light transfer between crystal and photodetector using NOA 169 glue and unsealed photodiode. From the measurements it can also be noticed that, as expected, larger light collection, which implies lower losses, lead to greater energy resolutions.

The accuracy in peak position and FWHM determination, could be improved if the radioactive source was collimated and placed in a fixed position regarding the scintillator. This would direct the gamma photons and decrease random path fluctuations, improving energy resolution. In addition, the amplifier gain should have been kept constant for all the measurements.

6.3 Possible further improvements

This work aimed to identify, among the studied options, the best components to build a scintillator detector with better light collection and energy resolution. This goal was reached and the detector of experiment nº 7 was identified as the best combination. It includes GAGG:Ce scintillator, teflon wrapping, unsealed photodiode from S3590 series from Hamamatsu and NOA 169 glue from Norland Optical Adhesive optical matching medium. However, in order to optimize the light collection and energy resolution of this detector even further, additional measures can be taken in the future. In the next paragraphs, a discussion of extra light collection improvement techniques are presented first, followed by an analysis of electronic noise reduction.

Starting by the entry of incident particles in the crystal, to optimize their detection, it’s important that the crystal’s input face is clean and polished. Coatings, residues, and irregularities increase the loss of particles, especially heavy particles, on the entrance surface.

Regarding the scintillation photons collection, the medium between the crystal and the wrapping material and between the crystal and the photodiode must be an high refractive index (n) material. This is because, the higher the refractive index of this middle layer, the larger is the critical angle of the interface crystal-surrounding and a larger critical angle leads to more internal reflections in the lateral faces meaning less losses. In this work NOA 169 glue with n =1.69 was used, but is no longer manufactured. Optical adhesives with larger refractive index can be used, improving light collection. In addition, the whiter the teflon material used, the higher is its diffuse reflectivity and thus, the better is its efficiency at recovering photons.

On the other hand, as the collages were made by hand, it couldn’t be guaranteed that the collages were homogeneous, leaving air bubbles, although small, between optical interfaces. This fact could lead to less light collection and energy resolution that expected in some cases. One way to try to decrease air bubbles in the interfaces could be to subject the assembly to vacuum, while the NOA 169 glue is still liquid so that the bubbles collapse.

Regarding electronic noise, it is present in every experiment, which contributes to energy resolution degradation. Low energy noise was noticeable as a first peak in all spectra, however it was not presented in the Figures, as it presented no information of interest. One source of low frequency noise is the electronic processing unit. Flicker noise is a readout noise, which has a 1/f power spectral density, being present only in low energies. It is caused by charge carriers and typically occurs in semiconductors and, as such, it's decreased when semiconductor components amount is kept low. Also, hardware or software high pass filtering techniques can be applied to reduce low energy noise.

In addition to low energies flicker noise, all the frequencies face shot noise and Johnson-Nyquist noise produced by electronic processing unit noise and background radiation. Shot noise is derived from the quantum nature of particles and therefore cannot be eliminated. Johnson-Nyquist noise can be reduced lowering cable length, keeping low the amount of resistive elements and decreasing temperature.

Dark noise generated by the photodiode can only be reduced if temperature is decreased. However, since the purpose of our measurements are comparative, it's not expected that the conclusions would change due to these extra precautions. LYSO:Ce crystal presents, additionally, intrinsic radioactivity. This radioactivity is possible to be removed by software as well by subtracting the intrinsic spectrum, but it would require extra processing and measurements.

Chapter 7

Conclusions and Future Perspectives

7.1 Conclusion

The work developed through this project had two main focuses:

- Study of inorganic scintillators LYSO:Ce and GAGG:Ce as high energy radiation detectors
- Select components and mounting setup for an inorganic scintillation radiation detector in order to optimize light collection and energy resolution

Both objectives were achieved. First, the main characteristics of LYSO:Ce and GAGG:Ce were studied indicating that both inorganic crystals are adequate to space application high energy radiation detectors. The main reason for this are high stopping power for high energy photons, protons and fast electrons and the large light yield of the crystals, leading to high light output. However their high refractive index is one disadvantage once it leads to severe Fresnel losses in the interfaces with surrounding materials as vacuum and photodetector, which have much lower refractive index.

The high refractive index disadvantage can be circumvented by choosing a suitable mounting setup and materials associated to this crystals, generating a radiation detector, and this lead us to the second main goal of this work. Several candidate materials and components were evaluated for the photodetector, wrapping material and optical matching material, in terms of light collection efficiency and energy resolution. With the solution consisting on experiment nº 7, we obtained a scintillator detector that generates a current signal proportional to the energy deposited on the crystal, and thereby, in the first order, proportional to the particle incident energy.

The best detector solution has small dimensions (1 x 1 x 1.18 cm), good energy resolution (12.8 %), low noise level (110 keV) and high detection efficiency. This detector is composed by GAGG:Ce crystal, teflon wrapping with the setup of Figure 5.8, unsealed photodiode (Hamamatsu S3590-09) and NOA 169 glue as optical matching glue in the interfaces.

Despite the various precautions that need to be taken to properly mount the detector, for example to avoid leaving residues on the interfaces, the assembly of this detector is relatively easy to accomplish. In additon, teflon and SiPIN photodiode are cheap and commonly used. In contrast, NOA 169 glue is no longer manufactured. However, NOA 170 is available in Amstechnologies-webshop, which will provide even better results as the refractive index is 1.70 instead of 1.69.

In closing, it's important to highlight that the values of sensitivity and energy resolution measured in this work depend on the signal conditioning and signal processing systems used. The values achieved are the minimum values that we can guarantee with our detector, but other systems can add more, or less noise if their electronics are either more or less noisy than those used here. This means that it's crucial that in REPE application the signal conditioning system presents low noise, low consumption as well, added to an high amplification gain for all the expected bandwidth.

The scintillator detector discussed in this thesis, as a future part of REPE project, will contribute to the study of most abundant and dynamic particle population in the Van Allen radiation belts, i.e., electrons and protons.

7.2 Future perspectives

With the present work, scintillator detector components were studied and selected resulting on a small, good energy resolution and high efficiency scintillator. This detector includes the inorganic crystal GAGG:Ce, wrapped with teflon, associated to S3590 series SiPIN photodiode from Hamamatsu and NOA 169 by Norland Optical Adhesive as optical matching medium.

The selected combination was evaluated with gamma rays as incident particles, however the detector's main application is to detect energetic protons and electrons in REPE project, which will constitute the FORESAIL-2 CubeSat payload. The differences lie in the energy deposition by the incident particles. Protons and electrons will deposit their energy earlier in the scintillator, and will excite several crystal's electrons through all their track, instead of $\approx 100\mu$m sphere as assumed for gamma-rays. This means that, on contrary to gamma ray photons, protons and electrons detection imply extra care in the choice of crystal's face to place photodetector and to wrap. Photodetector should stay parallel to incident particles flux direction and no wrapping should be in particles path, in order to maximize energy absorption in the crystal and photons collection, presenting the same setup of experiment 7, shown in Figure 5.8. This means, experiment 7 should be the ideal setup for relativistic and ultrarelativistic particles.

On the same token, one crucial future step is to experimentally analyze Birks effect and crystal light yield of experiment 7, but this time with a proton beam as incident particles. This analysis is planed be performed in the accelerator of Kumpula Science Campus of the University of Helsinki, where protons can be accelerated up to 10 MeV.

The FORESAIL-2 CubeSat, where the REPE project will be inserted, will orbit the Earth and during this orbit, the temperature range is large, from about -10 ºC to +50 ºC. Therefore, an important future step is to study the behaviour of the detector with temperature variations. It's expected that the GAGG:Ce crystal light yield varies with temperature. This is caused by the fact that in scintillation crystals, radiative transitions, responsible for the production of scintillation light, compete with nonradiative transitions (quenching). In most scintillation crystals, quenching increases at higher temperatures, decreasing light output. In addition, the behaviour of glue at those temperatures must be tested.

In order to apply the selected detector in REPE project and reach accurate results, one signal processing system unit has to be added to it. This system's main objectives are to amplify the signal from the photodiode in order to be converted to digital next. In addition, one signal processing unit is needed to perform the analog to digital conversion in a ADC system and to extract interest information from the data, digitally, as for example pulse height, associate it to time information and save the data. Therefore, the second main future step associated to this work is to develop a signal conditioning system consisting of a preamplification circuit which as to be high gain, low noise, low consumption, temperature resistant and with small dimensions.

According to REPE requirements, the signal conditioning system must generate a voltage signal, proportional to the incident energy, with values between 0 and 1.8V. The noise shall by lower than 300 keV, the power in order of few tens of mW, the components shall resist a temperature range from -10 to 50 ºC, and operate within a bandwidth from 10 kHz to 1 MHz. To reach this requirements, a Charge Sensitive Preamplification (CSP) circuit similar to the one proposed in [24] can be used. This circuit limits the noise generated by the active components, improving the signal-to-noise performance of a preamplifier. It is done by a reduced number of active components being used. It is constituted by a low noise single-transistor transimpedance preamplifier and a voltage amplifier with a T feedback network. The CSP suggested by [24] allows a transimpedance of 120 dBΩ in a bandwidth from 1 kHz to 1 MHz. This circuit is presented in the Figure below top and the transimpedance at bottom.

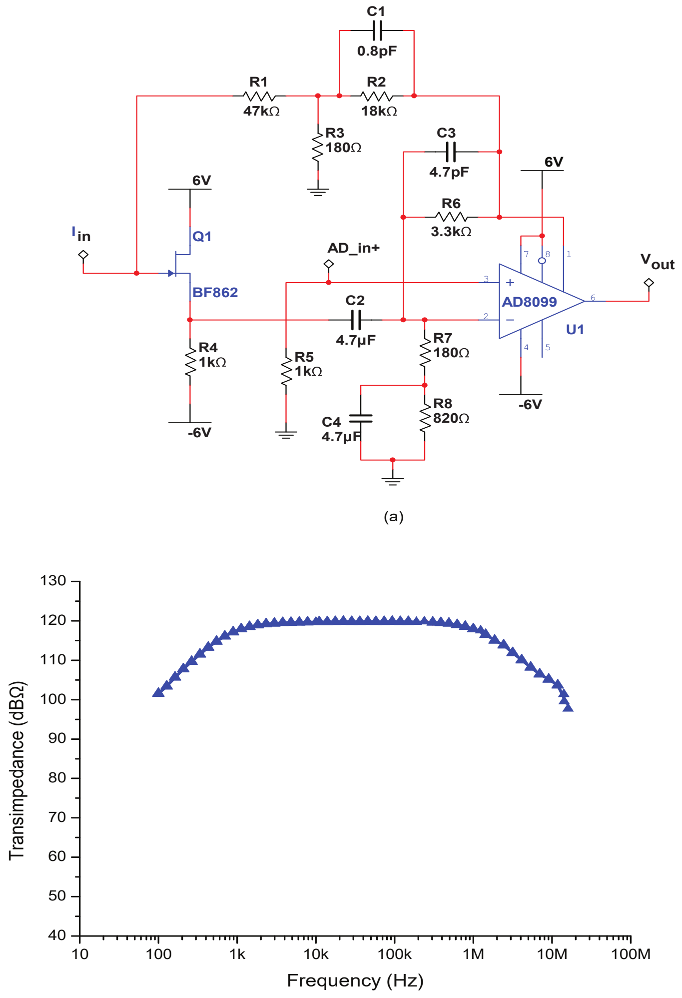

(a)

(b)

Figure 7.1: CSP circuit (a) and corresponding transimpedance as function of frequency (b). Image from [24].

The circuit is constituted by a first stage which converts the current from photodiode into a voltage signal using a JFET and a feedback loop, and a second stage consisting of a common-source voltage amplifier is used as the main amplification stage. It uses an ultra low noise N-channel junction FET from BF862 series by NXP Semiconductors, with a noise of 0.8 nV/$\sqrt{Hz}$. This JFET is no longer manufactured, thus a 2SK2394-6-TB-E JFET by ON Semiconductor can be used instead, which retains the most important features such as low noise. The T feedback loop allows a large transimpedance without compromising the bandwith, by using three small value resistors, instead of one unique large resistor. Another advantage of using small resistors is the decrease of Johnson-Nyquist noise, which is proportional to resistance value.

To ensure that noise is limited as much as possible, some key practical considerations must be taken into account when designing the PCB of the above circuit. First of all, the signal traces must be the as short and thin as possible, keeping the components close to each others, to reduce parasitic inductance. Inductance is inversely proportional to the logarithm of the diameter, and directly proportional to its length. If necessary, via holes can be inserted to keep traces short. In addition, the distance between adjacent traces should also always be greater than their width, thus reducing the risk of crosstalk (signal influence on the behavior of a signal that travels an adjacent trace).

Second, two decoupling (or bypass) capacitors in parallel, one larger and one smaller must be added between supply voltages and the ground. They should be placed as close as possible to each power pin of the active components, thus reducing current spikes during signal switching. In addition, multilayer PCBs are generally preferable, as they allow for separate layers for ground, power, and signals. This method reduces the common impedance coupling between the various subsystems. Furthermore, traces carrying power signals should be parallel to ground traces wherever possible, generating itself a decoupling capacitor.

Besides these basic precautions to take in the design of the signal amplification PCB, other more detailed precautions should be studied in order to keep noise and signal distortions low, as well as filtering techniques, if needed.

Appendix - Light path schemes

Below are the schemes of the light path propagating from GAGG:Ce crystal for silicon grease Figure 4.5a and NOA 169 glue between the crystal and the photodiode Figure 4.5b.

Bibliography

[1] Ahmed, S.N., 2007. Physics and engineering of radiation detection. Academic Press.

[2] Anagnostopoulos, G., Rigas, V., Vassiliadis, E., 2010. Radiation belt electron precipitation in the upper ionosphere at middle latitudes before strong earthquakes .

[3] Auffray, E., Frisch, B., Geraci, F., Ghezzi, A., Gundacker, S., Hillemanns, H., Jarron, P., Meyer, T., Paganoni, M., Pauwels, K., et al., 2013. A comprehensive & systematic study of coincidence time resolution and light yield using scintillators of different size and wrapping. IEEE Transactions on Nuclear Science 60, 3163–3171.

[4] Birks, J., 1964. The scintillation process in alkali halide crystals. IEEE Transactions on Nuclear Science 11, 4–11.

[5] Bizarri, G., Moses, W.W., Singh, J., Vasil'Ev, A., Williams, R., 2009. An analytical model of nonproportional scintillator light yield in terms of recombination rates. Journal of Applied Physics 105, 044507.

[6] Derenzo, S.E., Weber, M.J., Klintenberg, M.K., 2002a. Temperature dependence of the fast, near-band-edge scintillation from cui, hgi2, pbi2, zno: Ga and cds: In. Nuclear Instruments and Methods in Physics Research Section A: Accelerators, Spectrometers, Detectors and Associated Equipment 486, 214–219.

[7] Derenzo, S.E., Weber, M.J., Klintenberg, M.K., 2002b. Temperature dependence of the fast, near-band-edge scintillation from cui, hgi2, pbi2, zno:ga and cds:in. Nuclear Instruments and Methods in Physics Research Section A: Accelerators, Spectrometers, Detectors and Associated Equipment 486, 214–219. URL: https://www.sciencedirect.com/science/article/pii/S0168900202007052.

[8] Fukuda, M., 1998. Optical semiconductor devices. volume 46. John Wiley & Sons.

[9] Gramuglia, F., Frasca, S., Ripiccini, E., Descharmes, N., Charbon, E., Bruschini, C., Venialgo, E., Gate, V., Turover, D., . Light extraction enhancement techniques for inorganic scintillators, in: 2020 IEEE Nuclear Science Symposium and Medical Imaging Conference (NSS/MIC), IEEE. pp. 1–3.

[10] Hansson, C., Owens, A., Shortt, B., Dorenbos, P., Quarati, F., Williams, R., Hahn, D., Toepfer, T., Pathier, L., Schotanus, P., et al., 2012. Development of low noise scintillator crystals for planetary space missions, in: 2012 IEEE Nuclear Science Symposium and Medical Imaging Conference Record (NSS/MIC), IEEE. pp. 927–930.

[11] Heinrichs, U., Blume, A., Bußmann, N., Engels, R., Kemmerling, G., Weber, S., Ziemons, K., 2002. Statistical studies on the light output and energy resolution of small lso single crystals with different surface treatments combined with various reflector materials. Nuclear Instruments and Methods in Physics Research Section A: Accelerators, Spectrometers, Detectors and Associated Equipment 486, 60–66.

[12] Heynderickx, D., Quaghebeur, B., Speelman, E., Daly, E., 2000. Esa's space environment information system (spenvis)-a www interface to models of the space environment and its effects, in: 38th Aerospace Sciences Meeting and Exhibit, p. 371.

[13] Hui, R., O'Sullivan, M., 2009. Fiber optic measurement techniques. Academic Press.

[14] Jeong, M., Hammig, M., 2020. Development of hand-held coded-aperture gamma ray imaging system based on gagg (ce) scintillator coupled with sipm array. Nuclear Engineering and Technology 52, 2572–2580.

[15] Kim, C., Kim, D., Lee, Y., Park, C., Ullah, M.N., Kim, D., Kwon, I., Hur, S., Yeom, J.Y., 2021a. Radiation resistance and temperature dependence of ce: Gps scintillation crystal. Radiation Physics and Chemistry 183, 109396.

[16] Kim, C., Lee, W., Melis, A., Elmughrabi, A., Lee, K., Park, C., Yeom, J.Y., 2021b. A review of inorganic scintillation crystals for extreme environments. Crystals 11, 669.

[17] Knoll, G.F., 2010. Radiation detection and measurement. John Wiley & Sons.

[18] Koskinen, H.E., Kilpua, E.K., 2022. Physics of Earth's Radiation Belts: Theory and Observations. Springer Nature.

[19] Kramar, U., 2017. X-ray fluorescence spectrometers .

[20] Lai, S.T., Cahoy, K., Lohmeyer, W., Carlton, A., Aniceto, R., Minow, J., 2018. Chapter 16 - deep dielectric charging and spacecraft anomalies, in: Buzulukova, N. (Ed.), Extreme Events in Geospace. Elsevier, pp. 419–432. URL: `https://www.sciencedirect.com/science/article/pii/B9780128127001000169`.

[21] Lecoq, P., Gundacker, S., 2021. Sipm applications in positron emission tomography: toward ultimate pet time-of-flight resolution. The European Physical Journal Plus 136, 292.

[22] Leo, W.R., 2012. Techniques for nuclear and particle physics experiments: a how-to approach. Springer Science & Business Media.

[23] Li, W., Hudson, M., 2019. Earth's van allen radiation belts: From discovery to the van allen probes era. Journal of Geophysical Research: Space Physics 124, 8319–8351.

[24] Lin, T.Y., Green, R.J., O'Connor, P.B., 2012. A low noise single-transistor transimpedance preamplifier for fourier-transform mass spectrometry using a t feedback network. Review of Scientific Instruments 83, 094102.

[25] Locci-Lopez, D., Zhang, R., Oyem, A., Castagna, J., 2018. The multi-scale fourier transform.

[26] Min, S., Kang, H., Seo, B., Roh, C., Hong, S., Cheong, J., 2021. Integrated and portable probe based on functional plastic scintillator for detection of radioactive cesium. Applied Sciences 11. URL: `https://www.mdpi.com/2076-3417/11/11/5210`.

[27] NewAtlas, 2022. Nasa sending radiation belt storm probes to study the van allen belt. `https://newatlas.com/rbsp-solar-probe/23670/`. Accessed: 31-01-2022.

[28] Oleynik, P., 2021. PARTICLE OBSERVATIONS IN NEAR-EARTH SPACE: Design and verification of particle instruments for CubeSat experiments. Ph.D. thesis. University of Turku.

[29] Ozeki, T., Hara, E., 1976. Measurement of nonlinear distortion in photodiodes. Electronics Letters 12, 80–81.

[30] Products, N., . Norland products - adhesive index light sources and technical reports. https://www.norlandprod.com/adhesiveindex2.html. Accessed: 06-02-2022.

[31] Quinn, J., Hrebien, L., Leonid, 2022. Development of a pattern recognition approach for analyzing flow cytometric data .

[32] Reeves, G., Spence, H.E., Henderson, M., Morley, S., Friedel, R., Funsten, H., Baker, D., Kanekal, S., Blake, J., Fennell, J., et al., 2013. Electron acceleration in the heart of the van allen radiation belts. Science 341, 991–994.

[33] Roncali, E., Mosleh-Shirazi, M.A., Badano, A., 2017. Modelling the transport of optical photons in scintillation detectors for diagnostic and radiotherapy imaging. Physics in Medicine & Biology 62, R207.

[34] Sawyer, D.M., Vette, J.I., 1976. Ap-8 trapped proton environment for solar maximum and solar minimum. NASA sti/recon technical report n 77, 18983.

[35] Schotanus, P., Van Eijk, C., Hollander, R., Pijpelink, J., 1985. Temperature dependence of baf2 scintillation light yield. Nuclear Instruments and Methods in Physics Research Section A: Accelerators, Spectrometers, Detectors and Associated Equipment 238, 564–565.

[36] Seitz, B., Rivera, N.C., Stewart, A., 2016. Energy resolution and temperature dependence of ce: Gagg coupled to silicon photomultipliers. IEEE Transactions on Nuclear Science 63, 503–508.

[37] Sibczynski, P., Broslawski, A., Gojska, A., Kiptily, V., Korolczuk, S., Kwiatkowski, R., Mianowski, S., Moszyński, M., Rzadkiewicz, J., Swiderski, L., et al., 2017. Characterization of some modern scintillators recommended for use on large fusion facilities in γ-ray spectroscopy and tomographic measurements of γ-emission profiles. Nukleonika 62, 223–228.

[38] Enríquez-Mier-y Terán, F.E., Ortega-Galindo, A.S., Murrieta-Rodríguez, T., Rodríguez-Villafuerte, M., Martínez-Dávalos, A., Alva-Sánchez, H., 2020. Coincidence energy spectra due to the intrinsic radioactivity of lyso scintillation crystals. EJNMMI physics 7, 1–17.

[39] Uchida, N., Takahashi, H., Ohno, M., Mizuno, T., Fukazawa, Y., Yoshino, M., Kamada, K., Yokota, Y., Yoshikawa, A., 2021. Attenuation characteristics of a ce: Gd3al2ga3o12 scintillator. Nuclear Instruments and Methods in Physics Research Section A: Accelerators, Spectrometers, Detectors and Associated Equipment 986, 164725.

[40] Vette, J.I., 1991. The AE-8 trapped electron model environment. volume 91. National Space Science Data Center (NSSDC), World Data Center A for Rockets . . . .

[41] Wikipedia, 2022a. Fresnel equations — Wikipedia, the free encyclopedia. https://en.wikipedia.org/wiki/Fresnel_equations. Accessed: 08-June-2022.

[42] Wikipedia, 2022b. Pin-Diode — Wikipedia, the free encyclopedia. http://de.wikipedia.org/w/index.php?title=Pin-Diode&oldid=217245600. Accessed: 16-May-2022.

[43] Windows2universe, 2022. Charged particle motion in earth's magnetosphere precipitation of magnetospheric charged particles. https://www.windows2universe.org/earth/Magnetosphere/tour/tour_earth_magnetosphere_05.html. Accessed: 31-01-2022.

[44] Yamamoto, K., Fujii, Y., Kotooka, Y., Katayama, T., 1987. Highly stable silicon pin photodiode. Nuclear Instruments and Methods in Physics Research Section A: Accelerators, Spectrometers, Detectors and Associated Equipment 253, 542–547.

[45] Yoneyama, M., Kataoka, J., Arimoto, M., Masuda, T., Yoshino, M., Kamada, K., Yoshikawa, A., Sato, H., Usuki, Y., 2018. Evaluation of gagg: Ce scintillators for future space applications. Journal of Instrumentation 13, P02023.

[46] Zhuravleva, M., Stand, L., Wei, H., Hobbs, C., Boatner, L.A., Ramey, J.O., Shah, K., Burger, A., Rowe, E., Bhattacharya, P., et al., 2013. Hygroscopicity evaluation of halide scintillators, in: 2013 IEEE Nuclear Science Symposium and Medical Imaging Conference (2013 NSS/MIC), IEEE. pp. 1–5.